Broadband Passive Devices for Silicon–on–Insulator Platform

Heba Tamazin

Department of Electrical & Computer Engineering
McGill University, Montreal

April 2020

A thesis submitted to McGill University in partial fulfillment of the requirements for the degree of Master of Engineering.

Abstract

Over the past years silicon photonics has received tremendous interest among researchers as well as industry due to its compatibility with the mature CMOS technology which enables low cost and high-volume production. Across the recent literature, many devices –active and passive– have been implemented on a Silicon-on-insulator platform as well as full systems-on-chip comprising multiple components on a single Silicon chip to realize a full system (e.g. coherent receiver).

In parallel, the ever-increasing capacity demand is driving the need towards utilizing more wavelength bands other than the C- and O-bands centered at wavelengths of 1550 and 1310 nm, respectively, which are traditionally used in optical communications for the last three decades. This in turn motivates towards a whole wave of research towards designing broadband "colorless" devices that are transparent to operating wavelength.

In Chapters 2 and 3 of this thesis, we design and fabricate on a Silicon-on-insulator platform an ultra-broadband adiabatic coupler and a 2×2 optical switch based on the proposed adiabatic coupler that operate over a simulation bandwidth of more than 350 nm which covers the O, E, S, C and L- bands and an experimentally verified operating bandwidth of 153 nm over which the resulting extinction ratio is 15 dB or better. We fully characterize the adiabatic coupler in terms of its operating bandwidth and splitting ratio. Also and the 2×2 switch is characterized in terms of its bandwidth, extinction ratio between output ports, switching time between bar and cross states as well as the electrical power needed for switching between its two operating states, i.e. the power consumption of the switch. Finally, we experimentally examine the effect of its finite extinction ratio on the system-level performance of a 50 Gb/s OOK transmitted live traffic data.

Finally, in Chapter 4 of this thesis, we perform a detailed study of another passive device; waveguide Bragg gratings on Silicon-on-insulator. In this study, we survey the theory of operation of grating structures as well as their main types, applications and design parameters. We perform full device simulation of a uniform Silicon photonic Bragg grating verifying its resulting Bragg wavelength and operating bandwidth.

Résumé

Au cours des dernières années, la photonique sur silicium a suscité un vif intérêt de la part des chercheurs ainsi que de l'industrie en raison de sa compatibilité avec la technologie CMOS, une plateforme mature qui permet une production à faible coût et à grand volume. Dans la littérature récente, de nombreux dispositifs - actifs et passifs - ont été intégrés sur la plate-forme silicium sur isolant (SOI). Des sous-systèmes comprenant plusieurs composants ont aussi été intégrés sur une seule puce en silicium afin de réaliser un système complet (par exemple, un récepteur cohérent).

En parallèle, la demande de capacité toujours croissante incite à utiliser davantage de bandes de longueurs d'onde, et non seulement les bandes C et O - centrées sur les longueurs d'onde de 1550 et 1310 nm respectivement - qui ont traditionnellement été utilisées pour les communications optiques au cours des trois dernières décennies. Ceci, à son tour, motive toute une vague de recherches orientées vers la conception de dispositifs «incolores» à large bande, transparents pour la longueur d'onde de fonctionnement.

Dans les Chapitres 2 et 3 de cette thèse, nous concevons et fabriquons sur la plate-forme SOI un coupleur adiabatique à très large bande et un commutateur optique 2 × 2 basé sur le coupleur adiabatique proposé, qui fonctionnent sur une largeur de bande supérieure à 350 nm en simulation, couvrant les bandes O, E, S, C et L. La largeur de bande de fonctionnement vérifiée expérimentalement est de 153 nm, sur laquelle le taux d'extinction est de 15 dB ou mieux. Nous caractérisons exhaustivement le coupleur adiabatique en termes de bande passante et de ratio de répartition. Le commutateur 2 × 2 est également caractérisé en termes de largeur de bande, de ratio d'extinction entre les ports de sortie, de temps de commutation entre les états ‘bar’ et ‘croisé’, ainsi que de puissance électrique nécessaire pour la commutation entre ses deux états de fonctionnement, soit sa consommation énergétique. Enfin, nous examinons expérimentalement l’effet de son ratio d’extinction fini sur les performances au niveau système, en transmettant en temps réel un trafic de données OOK à 50 Gb/s.

Enfin, au Chapitre 4, nous étudions en détail un autre dispositif passif: le réseau de Bragg en guide d’onde intégré sur SOI. Nous examinons la théorie de fonctionnement de ces structures, ainsi que leurs principaux types, applications et paramètres de conception. Nous effectuons la simulation complète d’un réseau de Bragg uniforme sur silicium en vérifiant la longueur d'onde de Bragg et la bande passante obtenues.

Acknowledgements

First, I would like to thank my advisor Prof. David V. Plant for his academic advice, guidance and support ever since I started my M.Sc. I feel extremely privileged for having been part of his research group. I am very grateful to Prof. Plant for giving me the opportunity to revive my career after a long pause following my undergraduate studies. Prof. Plant sets an example by working tirelessly to provide us with a productive research environment and a hands-on experience in a world class laboratory.

Also, I would like to express my gratitude to my colleagues who helped me when I joined the group. Many thanks to Eslam El-fiky for the discussions, suggestions and help with my first experiment and Maxime Jacques for the lab trainings. Thanks to David Patel, Yannick D'Mello and Amar Kumar for your automation efforts that made our lab experience easier. I would also like to thank the rest of the group, Yun Wang, Md. Samiul Allam, Michael Hui, Luhua Xu and Deng Mao for the discussions, suggestions and lab help.

Next, I would like to express my deepest gratitude to my parents for their support and guidance throughout my whole life. I would not have been able to accomplish all this without my mother's prayers and my father's support. Thank you for always putting us first and your unconditional love.

Also, I would like to thank my siblings Farah and Ahmed. Thank you for always being there for me and for your love and support.

I would also like to thank my lovely daughters: Farida and Laila Osman. Their lovely smiles are the sunshine in my rainy days. Thank you for your support and unconditional love. Your presence in my life helps me get through any tough days.

Finally, my amazing husband, Mohamed Osman. None of this would have been possible without your constant love and support. Thank you for all the help in the lab and even with home chores. Thank you for being understanding, supportive and patient. Thank you for believing in me when I did not believe in myself. I love you endlessly.

In the end, this thesis, with all its worth, is dedicated to my husband, my parents, my grandma and my two lovely daughters.

Heba Tamazin

April 2020

Table of Contents

List of Figures

List of Tables

List of Acronyms

AC	Adiabatic Coupler
BER	Bit Error Rate
DC	Directional Coupler
ER	Extinction Ratio
GC	Grating Coupler
MMI	Multi - Mode Interference
MPW	Multi – Project Wafer
MZI	Mach-Zehnder Interferometer
OADM	Optical Add Drop Multiplexer
ODC	Optical Dispersion Compensation
OOK	On – Off Keying
PPG	Pulse Pattern Generator
SiP	Silicon Photonics
SOI	Silicon - on – insulator
SWG	Sub-Wavelength Grating
TE	Transverse Electric
TIA	Trans - Impedance Amplifier
TM	Transverse Magnetic
VOA	Variable Optical Attenuator
WDM	Wavelength Division Multiplexing

Chapter One

Introduction

1.1 Passive Silicon Photonics – an overview

Over the past decade the growth in Silicon photonics (SiP) research and industry has been unprecedented. The attraction in using Silicon as a host material for photonic devices is due to its potential to realize highly performing photonic devices with small footprint, high yield and CMOS compatibility [1, 2]. The compatibility of Silicon device fabrication with the mature CMOS industry enabled high volume production of SiP devices at a low cost and brought this ever-growing technology inside data centers, in computing applications, bio-sensing and many other applications [3].

1.1.1 Why Silicon?

Silicon is an optically transparent material to the wavelengths that are conventionally used for optical communication (1.26 ~1.6 μm) which makes it an ideal platform for the realization of passive devices and optical waveguides. It is a promising platform that enables the integration of multiple devices – active and passive – on a single chip, i.e. a system on chip, hence eliminating the need for multiple chip-to-fiber and fiber-to-chip coupling stages which reduces the overall insertion loss of the system.

Silicon on insulator (SOI) platform is highly favorable due to the large index contrast between the core (Silicon) and clad (Silicon dioxide) material. This large index contrast provides higher light confinement, enables more compact devices and denser integration since it brings waveguide dimensions down to the submicron level. Hence, thousands of SiP devices can be implemented on a single chip which is more than any other photonic platform [2].

Another major advantage is its compatibility with the mature CMOS process which has been used for electronics for many decades. This compatibility provided public access to fabrication runs which allowed students, researchers and developers to design, fabricate and test multiple SiP devices that can go from research straight to large volume production. This is in contrast to other integrated optics platforms (e.g. indium phosphide (InP)) in which wafers are very expensive and hence its fabrication runs are not readily available for students and developers to use. Moreover, the idea of monolithically integrating electronics and photonics on the same chip would allow seamless transfer of information from the optical to electrical domain and vice versa with better performance, low cost and high scalability. With monolithically integrated electronic and photonic components, there is no need to perform any interconnection through bandwidth limiting wire bonding or flip-chipping between the photonic and electronic chips ultimately resulting in electro-optic and opto-electronic devices with wider bandwidths [4]. On the other hand, one can argue that monolithic integration of photonics and electronics is a waste of resources and, from an economic point of view, is very inefficient since SiP requires a primitive process if compared to the advanced electronics fabrication process [3]; there is a huge disparity in minimum features sizes required for photonic devices and transistors.

Furthermore, the discovery of the plasma dispersion effect by Soref and Bennett; which revealed the effect of varying the carrier concentration in silicon through applying an electric field has opened the door to optical modulation in Silicon [5]. Since the applied electric field causes a change in the carrier concentration which induces a change in the refractive index thus enabling optical phase modulation. Ever since their published work in 1987, multiple SOI modulators were demonstrated such as a 50 GHz Silicon micro-ring modulator by Intel [6] and travelling wave SOI Mach-Zehnder modulator of an electro-optic bandwidth of 41 GHz [7] enabling 128 and 112 Gb/s PAM4 transmission, respectively. Photodetectors (PDs) on SOI were also realized using Germanium-doped silicon [8] and Graphene-Silicon heterostructure [9] as examples.

On the other hand, Silicon has a primary limitation in not being able to host native Silicon lasers and optical amplifiers due to its indirect bandgap structure which limits its radiative recombination to an extremely low rate. Many efforts have been reported in this regard, whether using hybrid integration by bonding a III-V laser to the chip and using it as the photon source or using monolithically integrated quantum dot lasers on Silicon [10].

Another drawback of Silicon is the high birefringence of Silicon waveguides, where each polarization has a slightly different propagation constant hence circuits that use both polarizations require the use of polarization diversity concept. The SiP circuit is replicated and each copy is used to manipulate a single polarization then both polarizations are combined once again before coupling light from the chip.

Furthermore, the large thermal coefficient of Silicon implicated temperature variations of SiP devices which would require thermal feedback mechanisms to overcome their temperature dependence. However, integrating such feedback mechanisms would definitely increase both the cost and complexity of SiP based systems. Nevertheless, this temperature dependence is sometimes beneficial for realizing thermal phase shifters on SOI which are used by different devices such as optical switches and modulators. Moreover, they are useful for thermal tuning of devices such as Bragg gratings and rings to the required operating wavelength.

1.1.2 Silicon waveguide design

As light (which is an electromagnetic wave) travels through a rectangular waveguide, the wave is either transverse electric (TE) or transverse magnetic (TM) depending on the direction of the wave relative to the plane of incidence. TE mode is when the electric field of the propagating wave is perpendicular to the plane of incidence (to the substrate). Conversely, the TM mode is when the magnetic field of the wave is perpendicular to the plane of incidence (to the substrate). TE and TM mode profiles in a silicon strip waveguide of 500 nm width are shown in Figure 1. It can be noted from the figure that the TE mode is confined in the center of the waveguide, while in the TM mode most of the power is concentrated along the interface between the Silicon and the oxide. For all the work done in this thesis, we focus on the fundamental TE mode only for our designs.

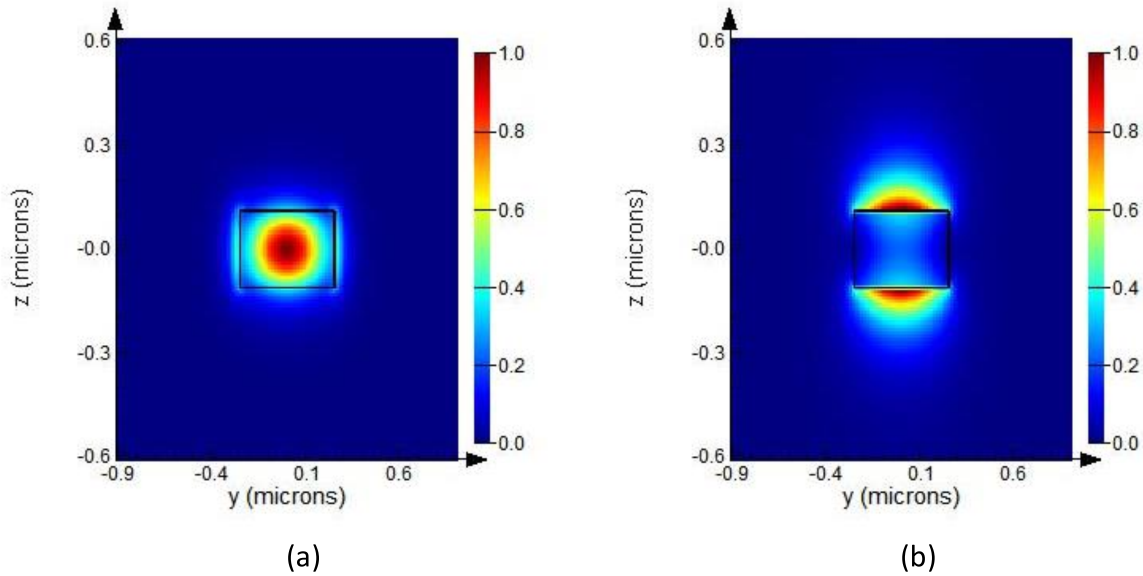

Figure 1. Mode profiles in a Silicon strip waveguide of width 500 nm with oxide cladding (a) TE mode (b) TM mode

Having the thickness of the waveguides set by the standard fabrication process as will be shown in the following section, the designer can vary the length and width of the waveguide as desired depending on the application. The waveguide width and thickness affect the effective index (n_{eff}) of the waveguide which in turn also affects the allowable guided modes inside the waveguide. Also, the effective index of the waveguide is wavelength dependent thus the choice of the waveguide width depends on the desired operating bandwidth. Figure 2 (a), (b) shows the effective index of different waveguide modes at different waveguide thicknesses of a Silicon strip waveguide for both the C- and O-bands, respectively. Hence, for single mode operation (when only the fundamental TE or TM mode are supported), the chosen waveguide width must be less than 500 nm or 400 nm for C- or O-band operation, respectively.

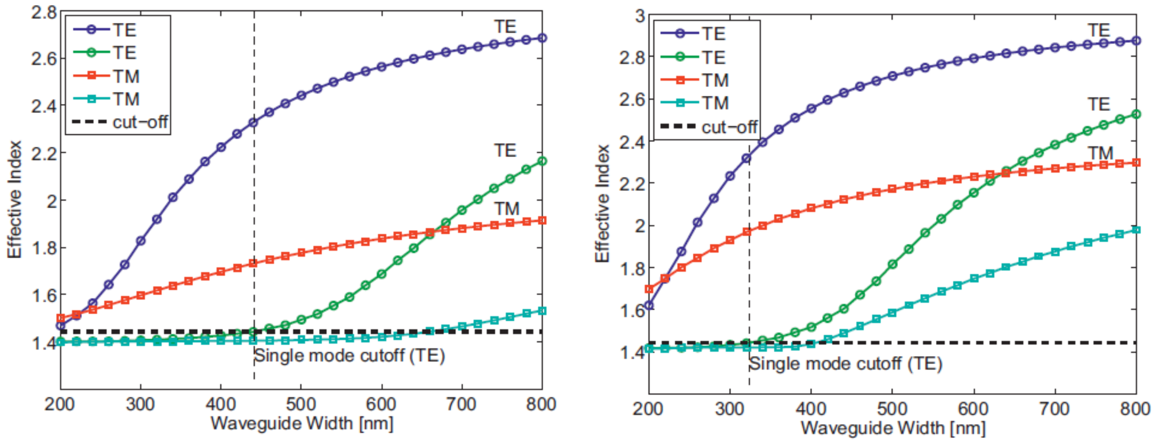

(a) (b)

Figure 2. Effective index of different waveguides modes at various waveguide thicknesses at (a) 1550 nm and (b) 1310 nm. Figures excerpted from [3].

In the O-band the mode profile is tighter so a narrower waveguide would be appropriate for use, while in the C-band, the mode profile is larger and hence a wider waveguide width is used since using a very narrow waveguide would cause large losses due to the mode interaction with the sidewalls. This is the reason behind the conventionally used widths for strip waveguides which are around 500 nm in the C-band and 350 nm for the O-band. The choice of waveguide thickness to enable joint operation in both the O- and C- bands thus needs to be carefully considered to avoid incurring large losses, it will be one of our design considerations as we will explain in Chapter 2. It is worth noting that symmetric waveguides (with Silicon dioxide cladding) always have a guided mode which is the fundamental mode, however for asymmetric waveguides (e.g. with an air cladding) the fundamental mode is not necessarily guided.

There are different types of waveguides that are used in the SiP platform such as the strip, rib and photonic-crystal waveguides. The most typically used waveguide structures are the strip and rib waveguides. Each waveguide structure has its own advantages that should be considered depending on the application. For example, strip waveguides are conventionally used for routing waveguides since they possess the highest mode confinement and hence enable tighter bends with lower losses. On the other hand, rib waveguides are useful for realizing SiP modulators (or electro-optic devices in general) since the slab region can contain a deposited electrode to which the electrical signal is applied enabling interaction with the optical mode propagating through the rib section. We will further discuss strip and rib waveguide structures and their mode profiles in Chapter 4.

1.1.3 Fabrication

Silicon photonics wafers that are used conventionally are called “Silicon-on-insulator”. They are typically 8” wafers and consist of a Silicon substrate of 725 µm thickness, 2 µm buried oxide (or BOX) and a top layer of crystalline Silicon of 220 nm thickness hence the term SOI. The BOX is typically a Silicon dioxide layer which is usually 2 or 3 µm deep to ensure proper isolation between the Silicon substrate and crystalline Silicon. The 220 nm Silicon thickness where all the devices are defined has become a standard used by different multi-project wafer (MPW) foundries such as used A*Star IME, imec and LETI [3]. Figure 3 shows the structure of the typical layers used for SOI device fabrication with their standard dimensions. The thickness of the silicon substrate can also be varied using multi-level etching which allows two different etching levels other than the standard 220 nm thickness which are 70 nm and 150 nm as provided by imec and can also be seen in Figure 3. These are useful to realize rib waveguides and grating couplers. The cladding is either Silicon dioxide or air depending on the designer’s choice, some advanced post processing is also available.

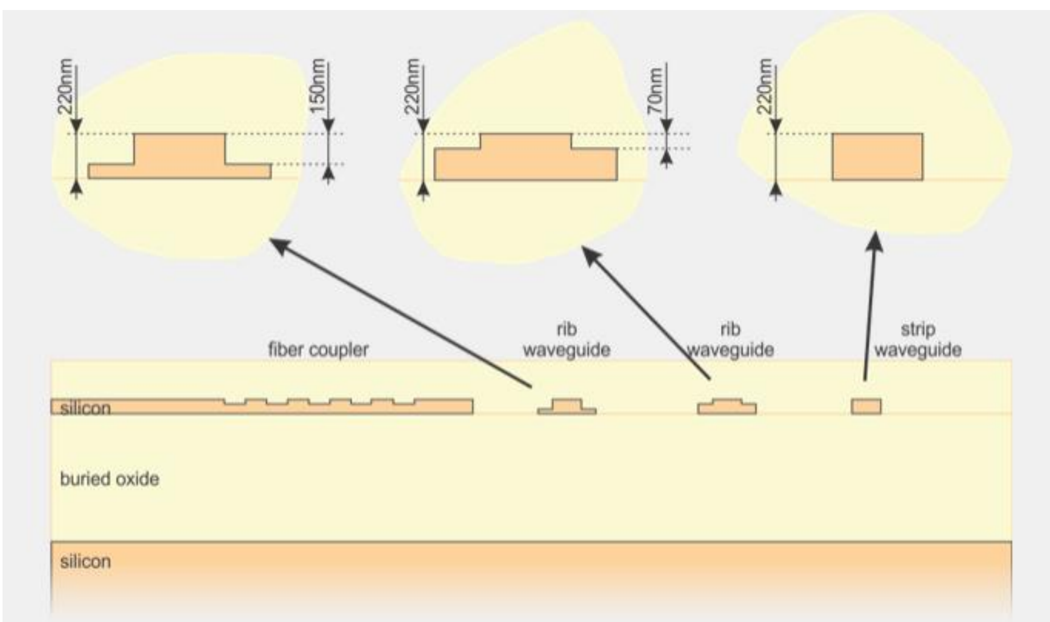

Figure 3. Cross section of Silicon photonics passives technology at imec excerpted from [11]

1.1.4 State of the art / Passive SiP devices

To date, many passive Silicon photonic devices were realized such as but are not limited to power splitters/couplers, waveguide Bragg gratings, polarization splitters rotators, grating couplers and hybrids.

Power splitters and couplers are basic devices that are widely used in SiP chips since they are a basic component that is found in switches, interferometric structures and various devices. Couplers have been realized using different structures where each structure has its advantages and drawbacks. The structure of choice has always been dictated by the application. Among the structures used are directional couplers which have a very small footprint however at the expense of a narrow operating bandwidth. Directional couplers that use both straight and bent waveguides have improved the overall bandwidth more than their conventional counterparts. In [12] a bent directional coupler with splitting of $3 \text{ dB} \pm 1 \text{ dB}$ is proposed over an optical operating bandwidth of 88 nm with an overall footprint of 20 µm × 3 µm. On the other hand adiabatic couplers and multimode interference couplers provide a large operating bandwidth but require a larger footprint. [13] reports an adiabatic coupler on SOI rib waveguides with a splitting ratio of 50.4%/49.6% over an operating bandwidth of 100 nm and the length of the coupler is 150 µm. A 3 dB multi-mode interference coupler whose footprint is 3.6×11.5 µm^2 and an operational bandwidth of 100 nm was also reported in [14].

Waveguide Bragg gratings on SOI are another widely used devices for filtering applications where the desired wavelength of operation or their operation bandwidth can be tailored by adjusting the grating period and corrugation depth. Tuning the Bragg wavelength of the fabricated device is also possible by using a thermal phase shifter. Waveguide Bragg gratings are used in optical add-drop multiplexers (OADMs) for WDM applications and as bio-sensors [15]. In [16], an ultra-compact OADM using misaligned sidewall Bragg gratings is proposed using both a single-stage and a cascaded configuration. It reports a 3 dB bandwidth of 6 nm and extinction ratios of 25 dB and 51 dB for single and cascaded configurations, respectively.

Furthermore, polarization splitters - rotators (PSRs) are crucial to solve the aforementioned birefringence problem in Silicon using polarization diversity technique where the incoming light is split into two polarizations (TE and TM). Since most of the SiP devices are designed for TE operation, the TM mode is usually rotated to become TE when coupling light into the chip. Next, the TE mode is further manipulated and propagates along the chip till it is rotated back to its original TM polarization state once again before being combined once again with the TE mode and coupling them from the chip into the output fiber. An example of a PSR on SOI that achieves a 20 dB extinction between both polarizations over a bandwidth of 50 nm is found in [17].

Finally, one of the most important SOI structures are grating couplers (GCs) which enable light coupling from optical fibers into and from the SiP chip. Many efforts were done to realize GCs that enable broadband operation while minimizing the insertion loss and maximizing the coupling efficiency. However, it was not yet possible to realize an ultra-broadband GC that operates over the O- and C- bands simultaneously hence designers opted for an optimized GC for operation in each band separately. [18] and [19] are an example and report a peak coupling efficiency of -4.3 and -3.8 dB over the O- and C- bands, respectively.

1.2 Objective and thesis organization

Various SiP devices have been proposed, designed and fabricated on the SOI platform over the past decade. The capacity demand in data center applications has driven the implementation of efficient broadband devices to be used in optical interconnects. The motivation behind the work done in this thesis arises from this growth in bandwidth demand. The work in [20] which proposed an optical transceiver that operates “colorlessly” over the O-, E-, S-, C- and L-bands served as an inspiration to realizing an ultra-broadband switch that would operate over a very large bandwidth on Silicon-on-Insulator platform.

In this thesis, we study some of the passive Silicon photonic devices, namely adiabatic couplers, 2×2 switches based on the adiabatic coupler and waveguide Bragg gratings. We design and simulate the different devices prior to their fabrication. Furthermore, the fabricated devices are experimentally tested and characterized. This introductory chapter has provided an overview on Silicon photonics, several passive devices that were previously reported in the literature and the motivation behind the work done in this thesis.

In Chapter two, we explain our proposed ultra-broadband adiabatic coupler operating principle and design procedure along with its detailed dimensions. Next, we discuss the simulation procedure used to simulate the coupler efficiently. Finally, the adiabatic coupler is fabricated, experimentally tested and the results are presented. Our work on the ultra-broadband adiabatic coupler was published in [21].

In Chapter three, we propose a 2×2 ultra-broadband switch that uses the aforementioned adiabatic coupler as its building block. The 2×2 switch is designed, fabricated and experimentally characterized. A thorough characterization of the switch is presented which includes both a basic characterization and demonstration of the switch performance in a live traffic experiment. The switch characterization highlights the key performance metrics of the switch such as its operating bandwidth and extinction ratio. Furthermore, the live experimental quantifies the system level performance of the fabricated switch when operated in a 50 Gb/s OOK experiment.

In Chapter four, we review the basic concepts of Bragg gratings, their design parameters and perform simulations of the device. We perform device level simulations of Bragg gratings to extract their operating bandwidth and Bragg wavelength. Some applications of Bragg gratings are also discussed.

Chapter Five summarizes the work presented in Chapters two and three highlighting the main contribution of this thesis.

Chapter Two

Adiabatic coupler on SOI platform

Switches are an essential block that is found in various SiP circuits in order to route signals on chip in different applications. In this chapter, we demonstrate a 3-dB adiabatic coupler that is designed, fabricated and used as the building block of a 2×2 ultra-broadband SiP switch.

2.1 Introduction

Optical couplers are one of the most basic components of a photonic circuit used to split/recombine light. Among the basic devices widely used for optical power splitting in SOI are the directional couplers (DCs), adiabatic couplers (ACs) and the multimode interference (MMI) couplers. One main advantage of ACs over conventional DCs or MMI couplers is that they are less sensitive to wavelength and polarization variations and are more fabrication tolerant [22]. On the other hand, ACs typically have larger footprints compared to their counterparts; coupling lengths are customarily on the order of hundreds of micrometers while delivering broadband operation on the order of hundreds of nm [23, 24]. Thus, the existing tradeoff between bandwidth and device size has dictated the choice of the coupler to be used depending on the application requirements. For example, for applications where a small operating bandwidth is sufficient and the footprint is required to be as small as possible, a DC will be the best choice. Conversely if the footprint is not crucial and broadband operation is the main goal of the design, then the AC or MMI will be the optimum choice. However, there were no previous reports on ACs that operate in both the C- and O-bands jointly. Such a “colorless” device is an essential building block for a broadband optical transceiver that operates in both the O- and C- bands similar to the one reported in [20].

Table 1 lists some of the ACs that were proposed and fabricated on SOI platform using different structures such as strip and rib waveguides or using sub-wavelength gratings (SWGs) along with some of their key parameters. It is noteworthy that some of the work in Table 1 were published following our designed AC but are included here to provide an updated survey on ACs in the literature to the reader. Nevertheless, our proposed AC at the time of publishing had the smallest footprint for a strip WG AC and largest operating bandwidth to the best of our knowledge.

Table 1. Summary of some proposed 3-dB adiabatic couplers on SOI platform

Reference	Coupling length (µm)	Bandwidth (nm)	Power splitting ratio (dB)	Structure	Year
[25]	1000	~ 400nm	N/A	Strip WG	2006
[26]	200	1530-1640	N/A	Strip WG	2010
[13]	100	1500-1600	3 ± 0.65	Rib WG	2013
[27]	50	1490-1620	3 ± 0.3	SWG WGs	2016
[28]	75	1500-1600	3 ± 0.6	Strip WG	2018
[29]	25	1500-1600	3 ± 0.27	SWG Slot	2018

2.2 Design

The operating principle of ACs is converting the injected fundamental mode adiabatically into even and odd supermodes as stated using the coupled mode theory that is explained in [30]. This occurs in the coupling region where the two waveguides are separated by a very small gap that allows interaction (coupling) between the mode (light) and the waveguide nearby resulting in power exchange between both waveguides. However, there are considerations that should be considered for the AC design. Asymmetry must be introduced between the two input waveguides in order to avoid the excitation of higher order modes. Moreover, the taper lengths must be long enough to ensure that the power remains in the fundamental mode as the mode evolution occurs adiabatically. The splitting ratio of the coupler is determined by the widths of the output waveguides of the AC, i.e. for 3 dB splitting the output waveguides must be of the same width to ensure 50-50 splitting. It is noteworthy that if light is injected into the upper port of the AC, both outputs will be in phase. While if the mode is injected into the bottom port of the adiabatic coupler, a π-phase difference will exist between both output fields.

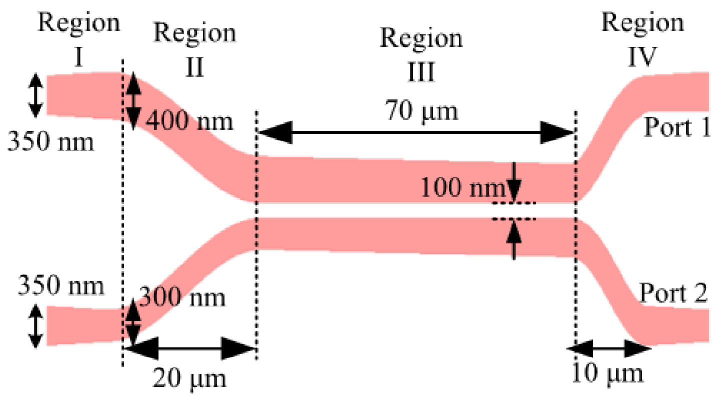

Figure 4. Adiabatic coupler design

The design of our adiabatic coupler is shown in Figure 4. In Region I, the input waveguides of the coupler of an initial width of 350 nm and spaced by 2 μm to avoid crosstalk between both ports. The two parallel waveguides are linearly tapered over 5 μm to 400 nm and 300 nm, respectively. We introduce the waveguide asymmetry in order to avoid the excitation of higher order modes. In Region II, two S-bends of length 20 μm are used to bring both waveguides together, the width of the S-bend remains the same over the entire 20 μm length. Next, in Region III (Coupling region), the two waveguides are linearly tapered to 350 nm (from the initial 400 nm and 300 nm), while maintaining a constant gap between both waveguides of 100 nm over a coupling length of 70 μm. Finally, two S-bend waveguides of length 10 μm are used to decouple the two parallel waveguides into the two output ports of the AC. The output waveguides are chosen to have similar widths to ensure 50-50 power splitting between both ports. The aforementioned parameters were chosen and optimized in simulations which are thoroughly discussed in the next section.

2.3 Simulations

ACs are relatively long devices whose simulations unless optimized and efficient have large memory requirements and would require a very long time. Thus, choosing the optimum waveguide widths for the tapers to be used and the coupling length of the AC through 3D finite-difference time domain (3D FDTD) method parameter sweeps is a tedious task. In order to avoid this exhaustive process, AC simulations were done on two steps.

First, preliminary simulations were done using the eigenmode expansion (EME) solver in Lumerical's commercial tool Mode. EME is suitable for very long devices whose geometry varies slightly along their length. The simulation region is divided into cells, where the geometry of the device does not change over the single cell. A larger number of cells is to be used in areas where there is a change in the geometry (i.e. in taper regions of the AC), the greater the number of cells the more accurate the simulation is (EME can better resolve the geometry) but of course at the expense of time and memory requirements. Waveguide widths were chosen to enable a broadband operation (in both O- and C- bands) while maintaining reasonable performance (losses). Waveguide widths less than 500 nm and 400 nm are commonly used throughout the literature for devices that operate in the C- and O-bands, respectively to guarantee single mode operation as was detailed in section 1.1.2. In the O-band the mode is more confined within the waveguide core, hence a smaller waveguide width can be used without incurring a lot of losses. Different waveguide widths in the range between 300 to 400 nm were simulated in order to find an intermediate width that simultaneously does not incur high losses in the C-band and maintain single mode operation in the O-band. A comprehensive parametric analysis was carried out using numerous values for the remainder of the design parameters (e.g. Coupling length, taper start and end widths and S-bend length), the values that yielded the best performance (in terms of losses, power splitting ratio, etc.) were chosen. It was found that a waveguide width of 350 nm provides the best performance over both bands for wave propagation throughout the interferometric structure. Moreover, different coupling region lengths were also simulated, namely 60, 65, 70, 75 and 100 microns. It was found that a 70 micron coupling region provided the best 50/50 splitting ratio with the shortest possible coupling region length given the 100 nm gap constraint between the two waveguides in region III which is due to the fabrication process used at the time. The full design parameters that were found to be optimal are clearly labeled in Figure 4 and detailed in section 2.2. After converging on the design parameters and dimensions to be used from EME simulations, the second step was to use 3D finite-difference time-domain (3D FDTD) method for simulating the AC with the chosen parameters using Lumerical FDTD. FDTD provides more accurate device simulations but require more time, so it was suitable for final broadband simulations to verify the AC performance once the design parameters were chosen.

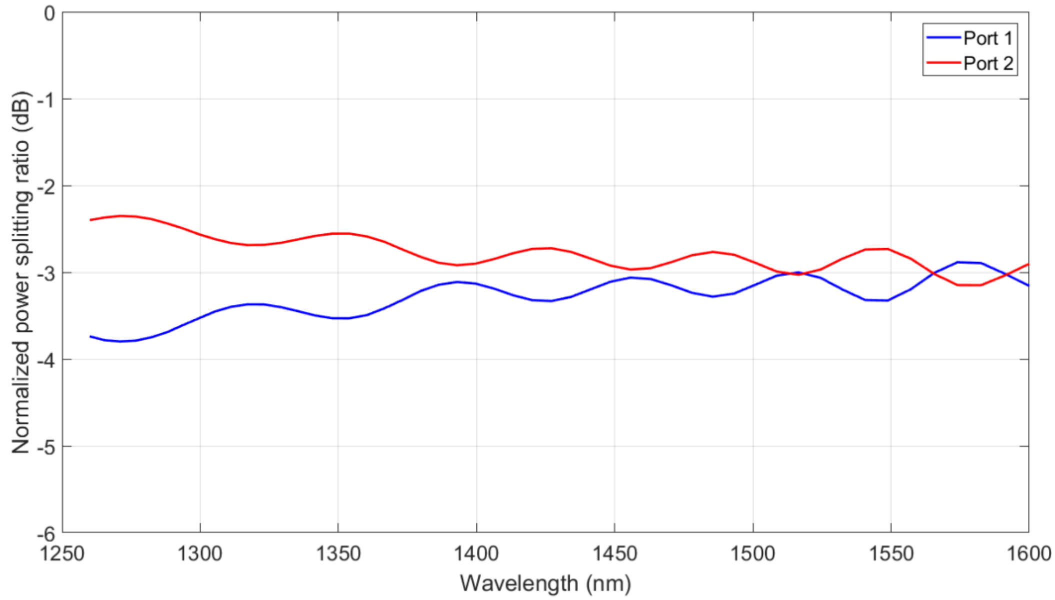

Figure 5. FDTD simulation results of the adiabatic coupler

Simulation results from FDTD of both ports of the AC are shown in Figure 5. Simulations show a power splitting of 3 ± 0.8 dB over 350 nm bandwidth covering the entire O-, E-, S- and C-bands.

2.4 Fabrication

The proposed AC was fabricated on a Silicon-on-insulator (SOI) wafer with 220 nm top Silicon thickness, 3 µm buried oxide (BOX) layer, and oxide cladding using single etch electron beam lithography (EBeam). In order to enable testing of our device, the designed AC was placed in a Mach-Zehnder interferometer (MZI) structure with a delay in one arm of the interferometer relative to the other to induce a free spectral range (FSR) of ~6 nm. A scanning electron microscope (SEM) image of the fabricated device is shown in Figure 6 showing the delay added to the lower arm of the MZI. Back-to-back grating couplers (GCs) were also fabricated near the device to decouple their response from that of the MZI structure to be tested. The GCs are individually optimized for either C- or O-band operation due to the absence of an ultra-broadband

GC that operates over the entire bandwidth of interest, whereas the MZI section including the input and output adiabatic couplers is kept the same.

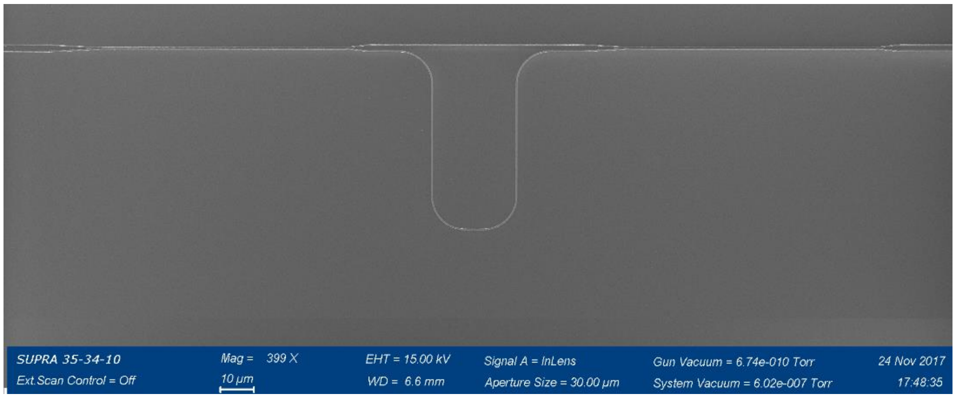

Figure 6. SEM image of the fabricated adiabatic coupler showing the imbalance in the lower arm of the MZI.

2.5 Experimental results

AC was tested using our automated test setup which comprises a fiber array, two Yenista TUNICS T100S-HP O- and C-band tunable lasers, and a CT400 passive optical component tester. The laser was passed through an off-chip polarization controller to adjust its polarization state to transverse electric (TE) for maximum power coupling to the chip. A fiber array unit was used to couple the laser into the chip through the input GCs and to extract the output from the output GCs into the optical component tester. The experimental setup structure is depicted in Figure 7 and a photo of the automated setup is shown in Figure 8.

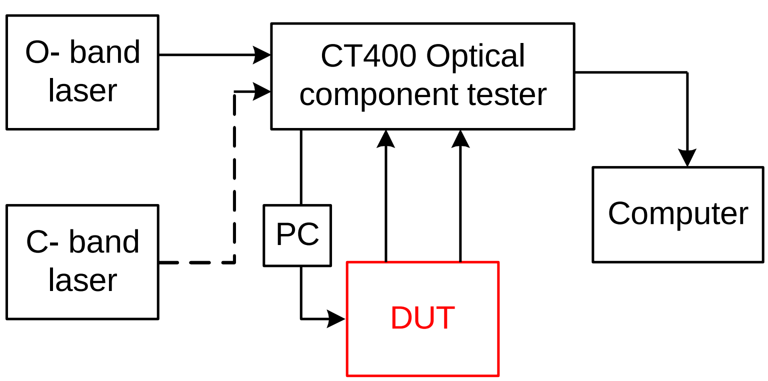

Figure 7: Schematic of setup used for AC testing. DUT: Device under test, PC: Polarization controller.

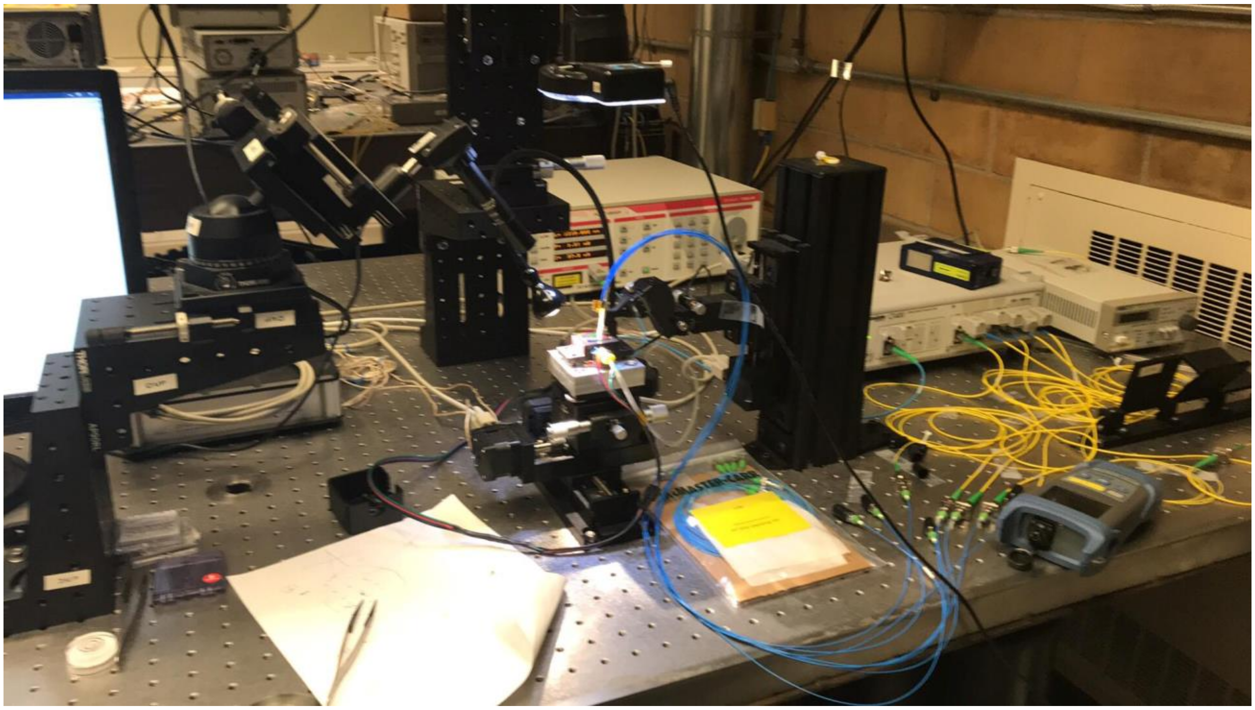

Figure 8: Photo of automated setup used for measurements

The power splitting ratio of the coupler at each wavelength can be extracted from the measured extinction ratio versus wavelength using the following equations adapted from [31]. Assuming a field splitting coefficient (k) for both the splitter and combiner ACs and lossless waveguides. The output fields (E_{out1} and E_{out2}) can be expressed using the transfer matrices as follows:

$$\begin{bmatrix} E_{out1} \\ E_{out2} \end{bmatrix} = \begin{bmatrix} \sqrt{1-k^2} & k \\ -k & \sqrt{1-k^2} \end{bmatrix} \begin{bmatrix} e^{-j\varphi_1} & 0 \\ 0 & e^{-j\varphi_2} \end{bmatrix} \begin{bmatrix} \sqrt{1-k^2} & k \\ -k & \sqrt{1-k^2} \end{bmatrix} \begin{bmatrix} E_{in} \\ 0 \end{bmatrix}$$

Where E_{in} is the input Electric field and φ_1, φ_2 are the phase shifts in both arms of the MZI and are equal to $\beta.L_1$ and $\beta.L_2$, respectively. β is the propagation constant, L_1 and L_2 are the lengths of each of the interferometer arms. We can express E_{out1} and E_{out2} as:

$$E_{out1} = \left[(1-k^2)e^{-j\varphi_1} - k^2 e^{-j\varphi_2}\right]E_{in}$$

$$E_{out2} = \left[-k\sqrt{1-k^2}e^{-j\varphi_1} - k\sqrt{1-k^2}e^{-j\varphi_2}\right]E_{in}$$

The power extinction ratios of both ports can be expressed as:

$$ER_1 = 10\ log_{10}\left(\frac{1}{1-4k^2(1-k^2)}\right)$$

$$ER_2 = \ 10\ log_{10}\left(\frac{4k^2(1-k^2)}{0}\right) = \ \infty$$

We can note from the previous equations that the coupler power splitting ratio is independent from ER_2 and it can be extracted from ER_1 and is given by:

$$K = \ k^2 = \frac{1}{2} \pm \frac{1}{2}\sqrt{\frac{1}{10^{ER_1/_{10}}}}$$

Where K is the power splitting ratio of the coupler, which can be easily calculated once the ER between the two output ports is measured from the experimental data at each wavelength.

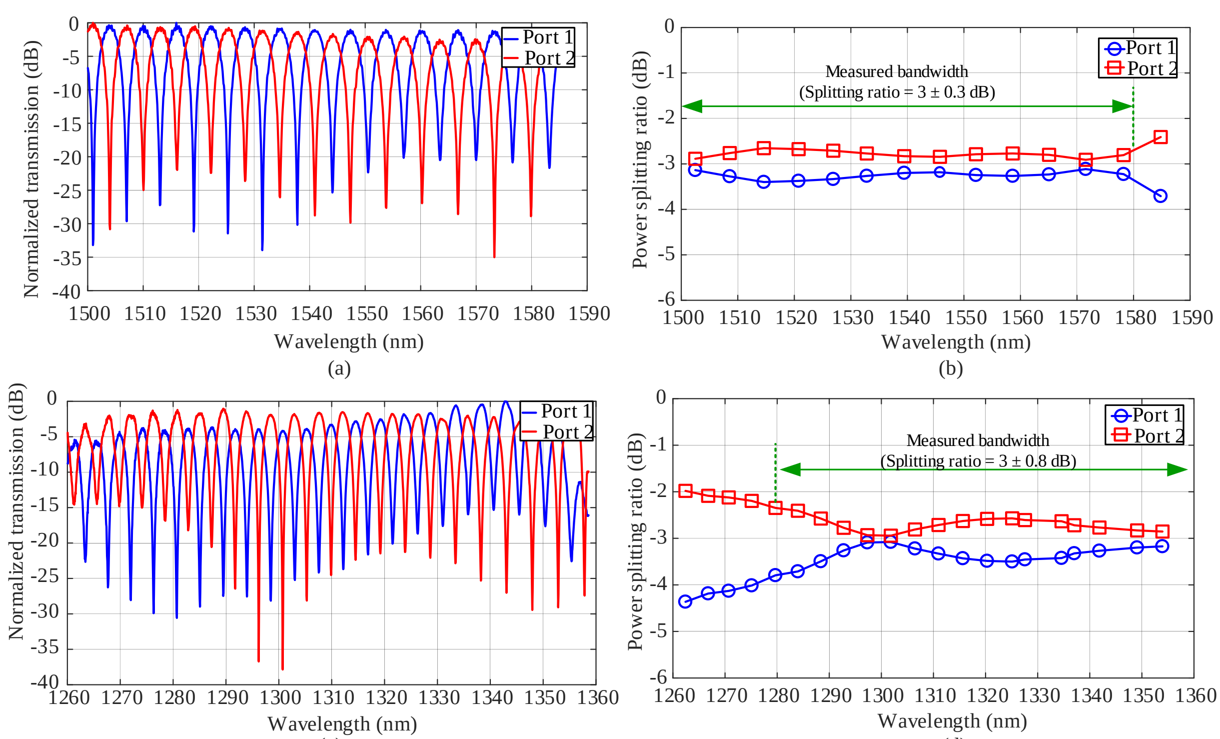

(a) (b) (c) (d)

Figure 9. Normalized power transmission versus wavelength at both output ports in (a) C-band, and (c) O-band, extracted experimental power splitting ratios of the proposed AC in (b) C-band, and (d) O-band.

Figure 9 (a) and (c) show the normalized measured output power on both ports of the MZI versus wavelength for both the C- and O-bands, respectively. From the extinction ratios, we extract the experimentally obtained splitting ratios shown in Figure 9 (b) and (d). These results confirm ultra-broadband operation with splitting ratio varying from the nominal 3 dB by less than ±0.3 dB over the band from 1500 to 1580 nm and by less than ±0.8 dB over the band from 1280 to 1360 nm i.e. an overall optical operating bandwidth of at least 160 nm. We could not measure the whole bandwidth covered in simulations (1260-1600 nm) due to unavailability of a laser source covering the whole range, however for the wavelength ranges measured experimental results are in good agreement with simulations. Hence, the AC should operate with reasonable performance over the entire simulation bandwidth of 350 nm, covering the O- E-, S- and C- bands.

2.6 Conclusion

In this chapter, we explained the design process of a broadband adiabatic coupler. Simulation tools were used in order to choose the design parameters of the coupler to achieve broadband operation over the O- and C- bands simultaneously with the same device. Simulation results for both ports of the AC showed a power splitting of 3 ± 0.8 dB over 350 nm bandwidth covering the entire O-, E-, S- and C-bands. The design was then fabricated on an SOI wafer with 220 nm top silicon thickness, 3 µm BOX layer, and oxide cladding using single etch EBeam process. The fabricated device was tested experimentally in the lab using tunable O- and C-band lasers and a power meter in which the laser was swept over both bands and the output power was recorded. The measured extinction ratios were then used to evaluate the coupler's splitting ratio. The full experimental setup and results were presented in section 2.5. Experimental results confirmed ultra-broadband operation with splitting ratio varying from the nominal 3 dB by less than ±0.3 dB over the band from 1500 to 1580 nm and by less than ±0.8 dB over the band from 1280 to 1360 nm i.e. an overall optical operating bandwidth of at least 160 nm has been verified experimentally.

Chapter Three

2×2 Ultra-broadband adiabatic coupler-based switch

In this chapter, we use the AC explained in the previous section as the building block of a 2×2 ultra-broadband switch. ACs were not widely used in SOI switches due to their large footprint, on the other hand switches based on DCs were more commonly used. The motivation behind the work done in this section is using the designed compact ultra-broadband AC to realize a 2×2 ultra-broadband switch with a total footprint comparable to other 2×2 switches reported in the literature that use other devices for power splitting and recombining.

3.1 Introduction

Among the various devices implemented on Silicon, optical switches are key devices that enable on-chip all-optical signal routing avoiding power hungry and lossy optical-to-electrical and electrical-to-optical conversion that would typically be required before and after an electronic switch if electronic switching implementation is chosen over an all-optical one. SiP based optical switches are essential building blocks for constructing network-on-chip systems for any on-chip inter-core communication inside high performance computers [32]. A 2×2 optical switch is the basic building block for implementing larger switching matrices that are required for routing optical signals between individual devices composing a SiP circuit, that is, to construct a network-on-chip. Switches based on interferometric structures were realized using different components for implementing the 3 dB input and output splitters such as bent directional couplers [33], directional couplers (DCs) [34], adiabatic bends [35] and Multimode interference (MMI) couplers [36, 37]. Many performance specifications of an optical switch need to be considered namely insertion loss, operating optical bandwidth, crosstalk and power consumption. Due to the dense population of the spectrum (especially the C- band), having an ultra-broadband “colorless” device that is suitable for operation in different communication bands is invaluable such as the transceiver proposed in [20]. Hence, an ultra-broadband 2×2 switch that operates “colorlessly” provides an essential block used in different applications in SiP circuits. However, the inevitable tradeoff between bandwidth and device footprint has dictated the choice of the splitter to be used. Directional coupler-based switches have a narrow bandwidth and small footprint, however broadband switches based on MMIs and ACs have a large bandwidth at the expense of a larger footprint. Multiple research efforts have resulted in switch designs that improve each of the aforementioned specifications. Some of these designs are summarized in Table 2 along with their key performance metrics in order to position the current work relative to the state-of-art across the literature. We notice that the highest reported bandwidth to date for 2×2 SiP switches is ~ 140 nm for the design in [33] that operates in C and L bands.

Table 2. Summary of performance metrics of previously reported switches.

Ref.	**Design used**	**BW**	**ER**	**Phase shift**	**Speed**	**Power consumption**
[33]	MZI with bent directional couplers	140 nm	> 20 dB	Thermo-optic	N/A	N/A
[34]	MZI with broadband DC	110 nm	> 17 dB	Electro-optic	4 ns	3 mW
[35]	MZI with adiabatic bends	70 nm	> 20 dB	Thermo-optic	2.4 µs	12.7 mW
[36]	MZI with MMI coupler	N/A	> 20 dB	Thermo-optic	4.25 µs (w/ trench) 1.19 µs (w/o trench)	24.9 mW (w/ trench) 54.4 mW (w/o trench)
[37]	MZI with MMI coupler	60 nm	> 17 dB	Electro-optic	6 ns	0.6 mW
[38]	Folded WGs in Michelson interferometer	N/A	> 26 dB	Thermo-optic	1.28 ms	50 µW
[39]	MZI with ACs	120 nm	> 15 dB	Thermo-optic	10 µs	N/A

This work	MZI with ACs	>153 nm	> 15 dB	Thermo-optic	13 μs	29 mW

In the following sections we explain the design and simulations done to realize an ultra-broadband 2×2 switch using broadband ACs and a thermo-optic phase shifter. In addition, we characterized experimentally the switching speed and the electrical power required for switching between the bar and cross states of the proposed switch. The effect of the finite extinction ratio of the switch on system performance is also finally assessed experimentally using 28 and 50 Gb/s On off keying (OOK) live traffic data by evaluating the bit-error-rate (BER) degradation in presence of crosstalk.

3.2 Design

A basic 2×2 switch design comprises two couplers for power splitting and recombination that are placed in a perfectly balanced interferometric structure. Our device is based on a conventional balanced Mach-Zehnder interferometer (MZI) with a phase shifter placed on one arm, an AC is used for power splitting and its mirrored copy is used for power recombination at the end of the MZI structure. Our design used a mirrored-image of the coupler for power recombination that was used conventionally in designing switches based on ACs such as in [39].

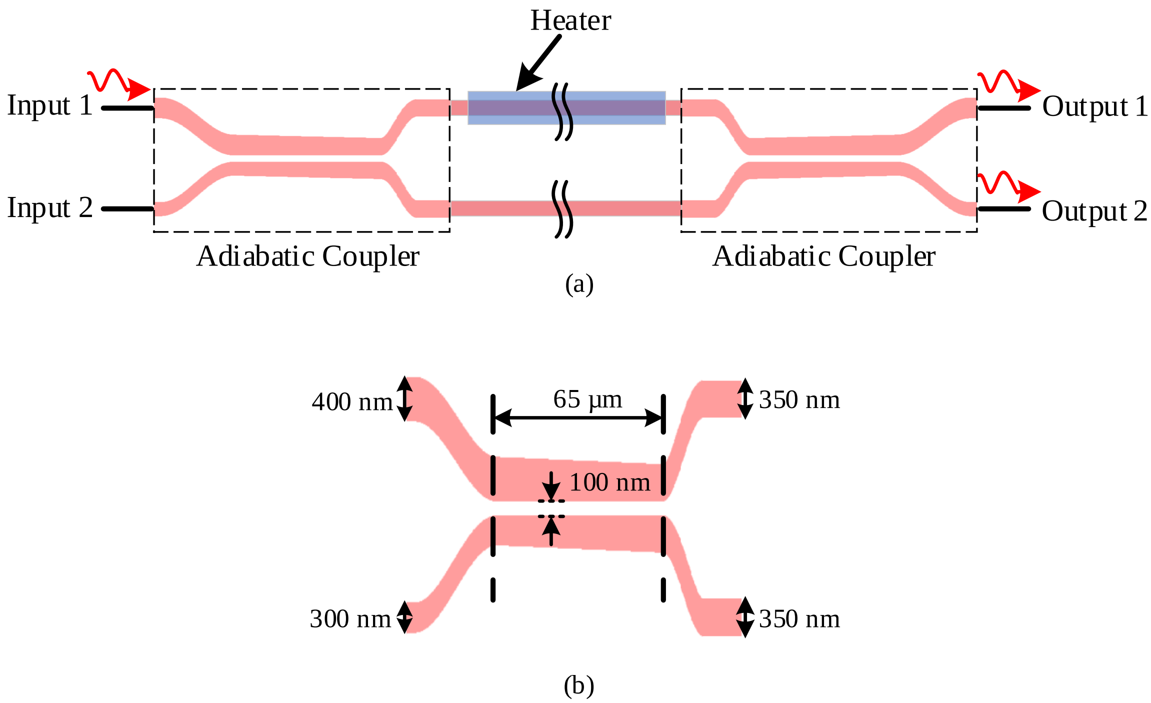

Figure 10. (a) Schematic of switch configuration / structure. (b) Schematic of adiabatic coupler design parameters.

An ultra-broadband AC is used for 3 dB splitting of the input power and its mirrored copy is used for recombining the power once again. The switch architecture as well as the detailed design of the AC are shown in Figure 10 (a) and (b), respectively. The input waveguide widths for the top and bottom ports were 400 nm and 300 nm respectively with a 2 μm initial separation. Next, the two input ports were brought closer together using S-bends of length 20 μm to reach a gap width of 100 nm. The 100 nm gap is then maintained throughout the coupling region where the waveguide widths change adiabatically over a length of 65 μm to reach their final width of 350 nm. The waveguide widths were adiabatically varied over 65 μm to ensure that higher order modes would not be excited, and that the power remained in the fundamental TE mode. Beyond the coupling length, the two waveguides were separated using S-bends of length 10 μm into both output ports of the AC. It is noteworthy mentioning that the AC used in the 2×2 switch is the same design with the same parameters that was presented in the previous chapter except for the coupling length. We used a coupling length of 65 μm here instead of the previously mentioned 70 μm since we found it still provides very good performance while saving 10 μm in the overall switch footprint. The waveguide width used for the MZI arms and for routing was 400 nm, which was chosen to be suitable for operation in both O- and C- bands. A 200 μm long thermal phase-shifter was placed in one arm of the MZI structure to control the switch operation, i.e. to set the switch in either the bar or cross states by applying an external voltage that induces a phase shift on one arm relative to the other based on the thermo-optic effect. This exploits the temperature dependent refractive index variation in silicon and induces a phase shift in the arm comprising the heater that is directly proportional to the applied voltage. The signal will be switched to the bar and the cross states when two arms of the MZI are in phase and out of phase, respectively.

3.3 Simulations

Simulations of the AC with the modified coupling length were done in the same manner as explained in section 2.3. An extra simulation step was added to facilitate the 2×2 switch simulations. Lumerical FDTD was used to extract the S-parameters of the AC over the entire wavelength of interest from 1200 – 1650 nm. Finally, the S-parameters of the AC were imported into Lumerical Interconnect to perform circuit-level simulations of the 2×2 switch. A tunable laser provides the input to the first AC which is placed in an MZI structure with its mirrored copy. A phase shifter is placed in one of the arms of the MZI to switch between bar and cross states of the switch. Finally, two power meters are connected to both outputs of the switch to capture the transmitted power versus wavelength. The full simulation layout used in Interconnect is shown in Figure 11.

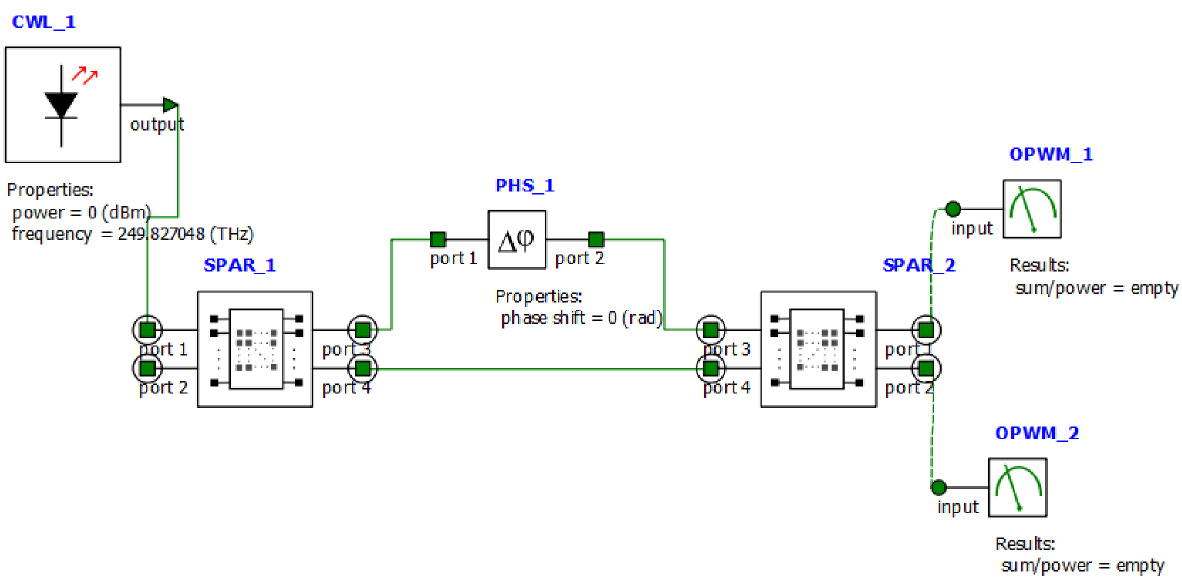

Figure 11. Schematic of circuit level simulations of the 2×2 switch using Lumerical Interconnect

The simulation results of the switch for the bar state when light was injected into input port 1 of the AC for both bar and cross states are shown in Figure 12 (a) and (b), respectively. Simulations show an extinction ratio of at least 15 dB achieved over an optical bandwidth of more than 350 nm in simulation that covers the O, E, S, C and L- bands.

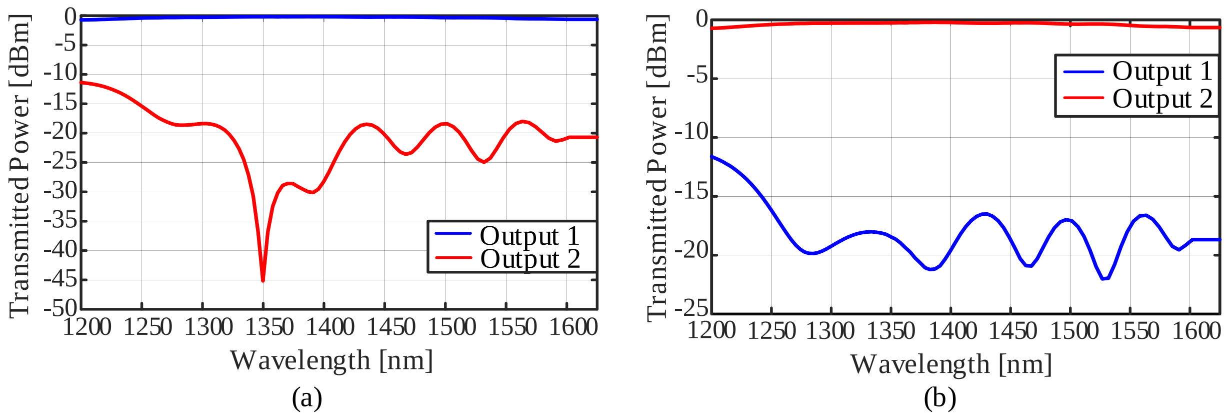

Figure 12. Simulated transmitted power vs wavelength of 2×2 switch in (a) Bar state and (b) Cross state for mirrored coupler MZI structure.

Unlike DCs, ACs are non-reciprocal devices since the accumulated phase is not the same in both paths due to the geometric nature of the device. Hence, a point of symmetry structure where the device is flipped along both vertical and horizontal axes is more suitable than mirroring the coupler to balance the MZI. Figure 13 (a) and (b) shows the schematic of the switch design using mirrored and point of symmetry structures, respectively. Using the point of symmetry MZI structure will decrease wavelength sensitivity and further improve the extinction between both ports as explained in [40]. The complete theory behind using point of symmetry to balance MZI structures is found in [41]. Unfortunately, the point of symmetry structure came to our attention after fabricating and testing the switch. However, we performed simulations to compare the performance in both cases (i.e. using point of symmetry or mirrored coupler) even though time did not permit fabricating both structures and testing them experimentally (only the mirrored coupler has been fabricated and tested as per sections 3.4 and 3.5).

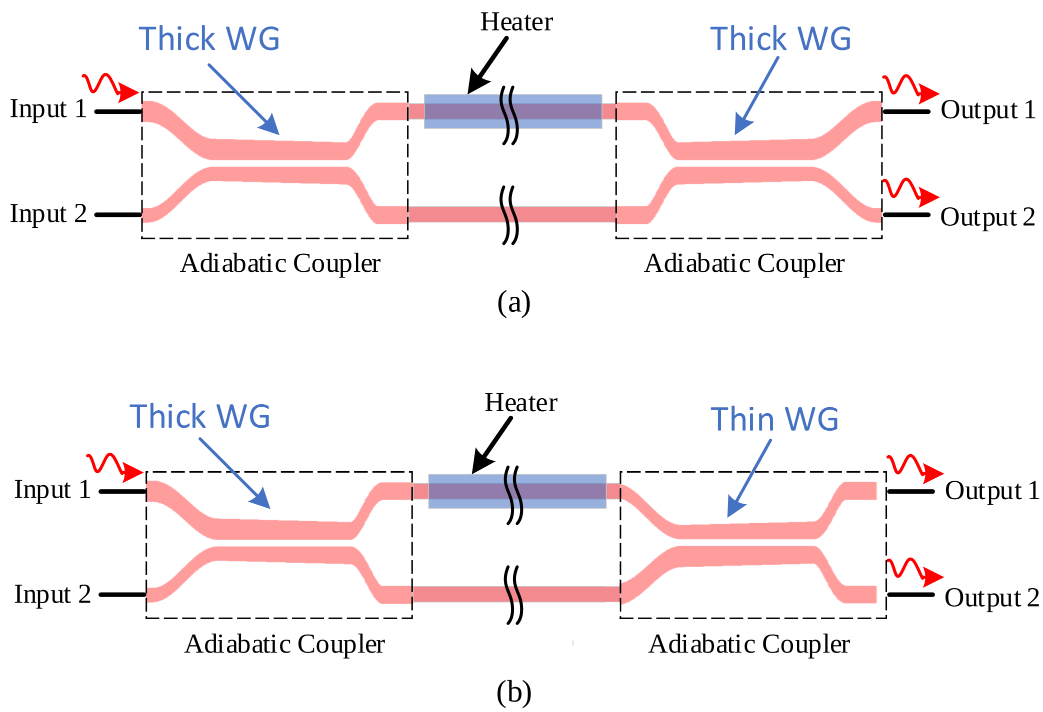

Figure 13. Schematic of switch design using (a) mirrored and (b) point of symmetry MZI structure.

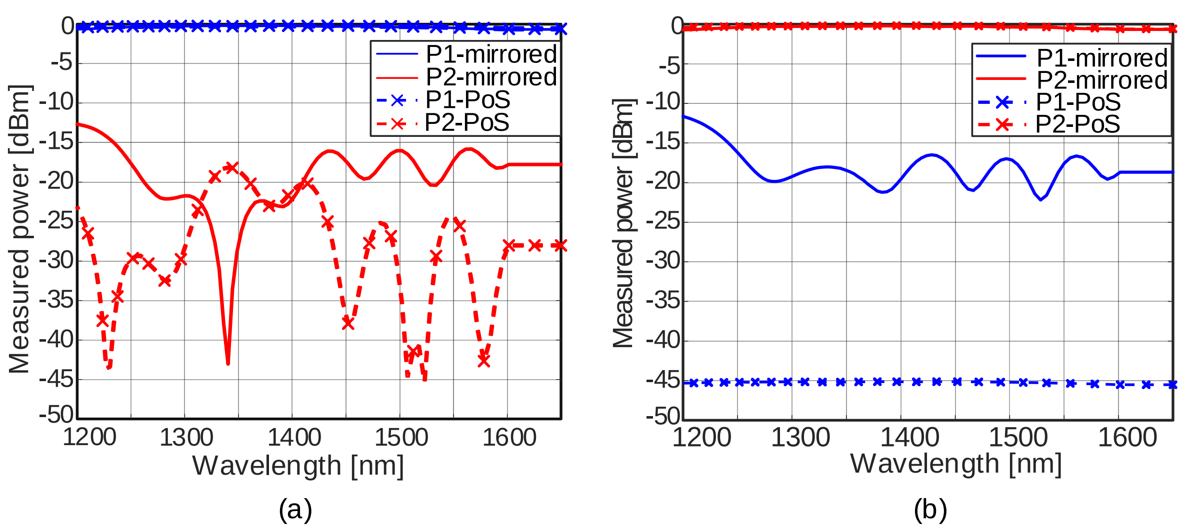

Figure 14. Simulation results showing comparison between point of symmetry MZI structure versus mirroring structure for (a) bar state and (b) cross state of the 2×2 switch. PoS: point of symmetry.

Figure 14 shows the simulated output power from the two ports of the switch versus wavelength for both the point of symmetry and mirrored coupler MZI structure. Both structures were plotted in the same figure for comparison, Figure 14(a) shows the bar state operation and

Figure 14(b) shows the cross state operation of the switch. Since ACs are non-reciprocal devices where the waveguides are asymmetric, there is a group delay difference between the two arms of the coupler due to the adiabatic change in the waveguide width which induces an effective index variation along the direction of propagation. Hence, point of symmetry structure is more suitable for such a device. In case of point of symmetry as depicted in Figure 13(b), the structure makes the two fields in the upper and lower arms of the interferometer more "matched" before they are combined by the output AC, since the field that passes through the thick waveguide in the input AC is passed through the thin waveguide in the output AC hence the overall phase accumulated remains almost the same. On the other hand, in the mirrored coupler case, the split electric fields accumulate different phases since the field passes through the thick (or thin) waveguide two times.

3.4 Fabrication

The proposed AC-based 2×2 switch was fabricated using electron beam lithography (EBL) and reactive ion etching (RIE) on a silicon-on-insulator wafer with 220 nm top silicon thickness, 2 µm buried oxide (BOX) layer and oxide cladding at Applied Nanotools Inc. The heater, which acts as a thermo-optic phase shifter, was fabricated using tri-layer metallization process and patterned by photolithography on top of the oxide layer to enable a compact heater with high resistance. The heater is made of a titanium-tungsten (TiW) alloy with an aluminum routing layer and a silicon dioxide protective layer. The protective oxide over the aluminum pads is then etched to allow for probing the heater. Light is coupled into and from the device using subwavelength grating (SWG) GCs. Due to the unavailability of ultra-broadband GCs that can couple light efficiently in both O- and C- bands simultaneously, the design was replicated identically and fabricated with broadband SWG GCs optimized for operation in the O- [18] and C-band [19] to enable testing the switch in both bands. The routing waveguides used between the device and the GCs were maintained to be 400 nm wide for both O- and C-band designs in order to ensure fair comparison of the switch performance in both bands. The total footprint of the device is 470 µm × 42 µm. Back-to-back GCs were fabricated adjacent to the grating couplers and their insertion loss measurement was used to de-embed their response from that of the device. A photo of the fabricated 2×2 switch is shown in Figure 15.

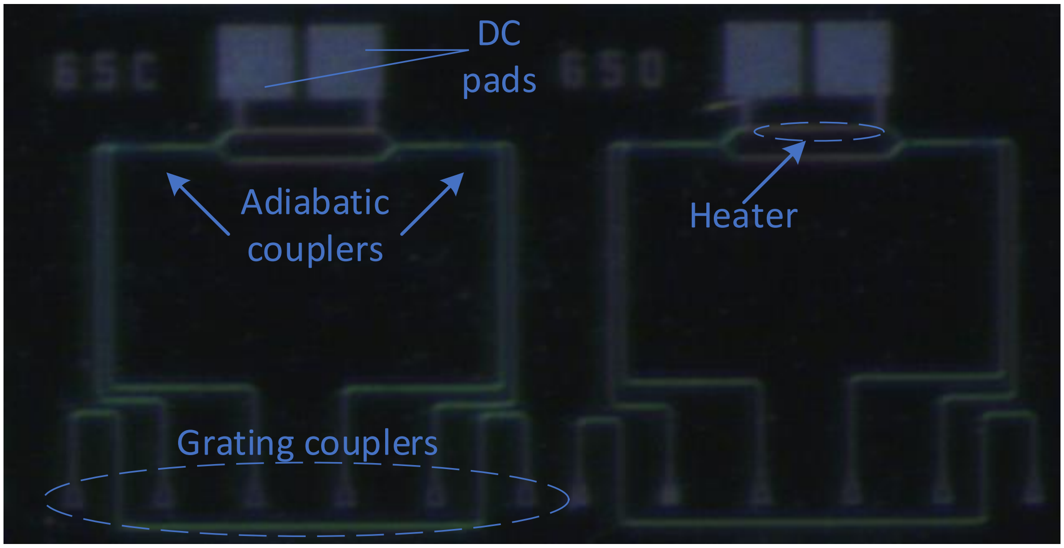

Figure 15. Picture of the fabricated 2×2 switch using Ebeam lithography.

3.5 Experimental setups and results

Experimental measurements of the 2×2 switch were done on two steps. First, we characterized the switch key performance metrics/parameters such as the optical operating bandwidth, switching speed, extinction ratio between both ports and the electrical power needed to switch between bar and cross operating states of the switch. Next, we transmitted live traffic (i.e. modulated data streams) through the switch and studied the effect of crosstalk from the undesired data on the desired data and BER levels that can be achieved.

3.5.1 Switch Characterization

As mentioned in section 3.1, among the key performance metrics of any switch are the bandwidth, extinction ratio and switching time. We first characterized the bandwidth and extinction ratio of the 2x2 switch using the setup depicted in Figure 16. First, a laser was used to provide the input CW light to the 2x2 switch through a fiber array unit. A DC supply was used to sweep the applied voltage on the thermo-optic phase shifter from 0 - 5V hence changing the phase shift between the two fields that will be combined at the end of the interferometer leading to a series of constructive and destructive interference patterns at each port. Therefore, by correctly driving the heater we can route the output to one of the two switch output ports i.e. operate in either bar or cross state. The optical output power from the two ports of the switch was recorded. Figure 17(a) and (b) show the output optical power versus the electrical power (the product of the applied voltage and the current drawn from the supply) dissipated by thermo-optic heater sweeps at 1310 nm and 1550 nm, respectively. We can conclude that the electrical power required to switch between the bar and cross states of the switch is 29 mW. The power consumption of the switch can be further improved by using trenches to isolate the two arms of the interferometer and reduce thermal cross-talk as proposed in [38].

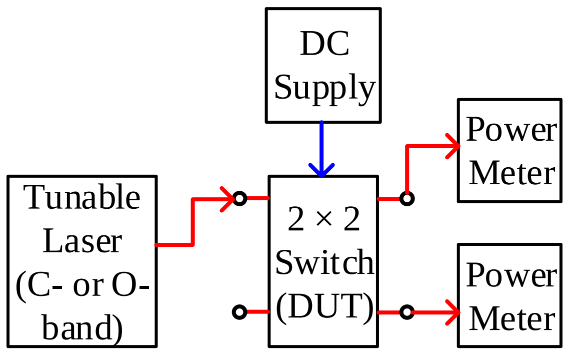

Figure 16. Experimental setup for switch characterization

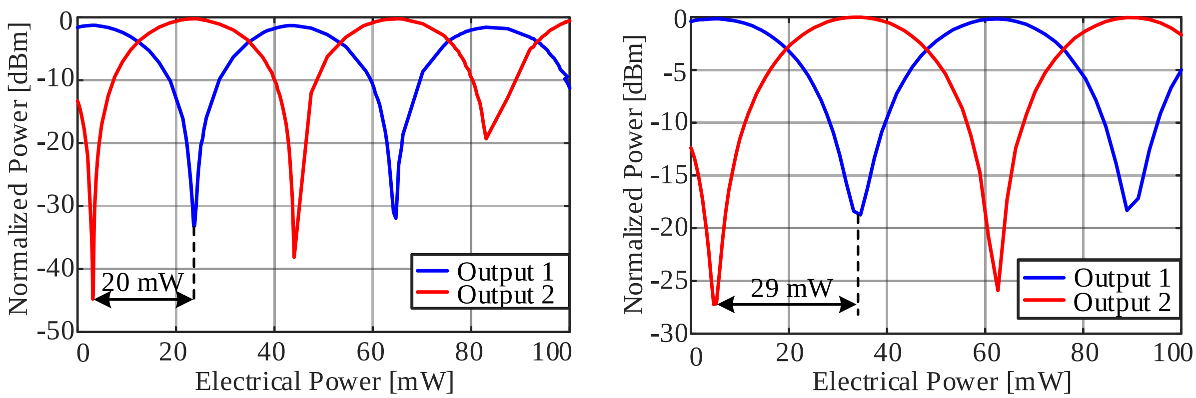

(a) (b)

Figure 17. Normalized output power from both switch ports at different applied electrical power on the heater at (a) 1310 nm and (b) 1550 nm input laser wavelengths.

Next, we extracted the ON and OFF voltage values from the aforementioned voltage sweeps, where the ON voltage is the voltage required for the switch to operate in its “Bar state” while the OFF voltage is the voltage required for the switch to operate in its ‘Cross state”. The same setup which was shown in Figure 16 was used here. The DC supply was used to apply V_{ON} and V_{OFF} on the heater to control whether the switch operates in the bar or cross state. Having the DC supply set to these specific values, we used a tunable O- band and C- band laser to sweep the wavelength of the input light while capturing the output powers of the switch ports using the two power meters. The resulting wavelength sweeps are shown in Figure 18, which shows the normalized output powers from both switch output ports at different wavelength values for both bar and cross operating states of the switch in the O- and C- bands.

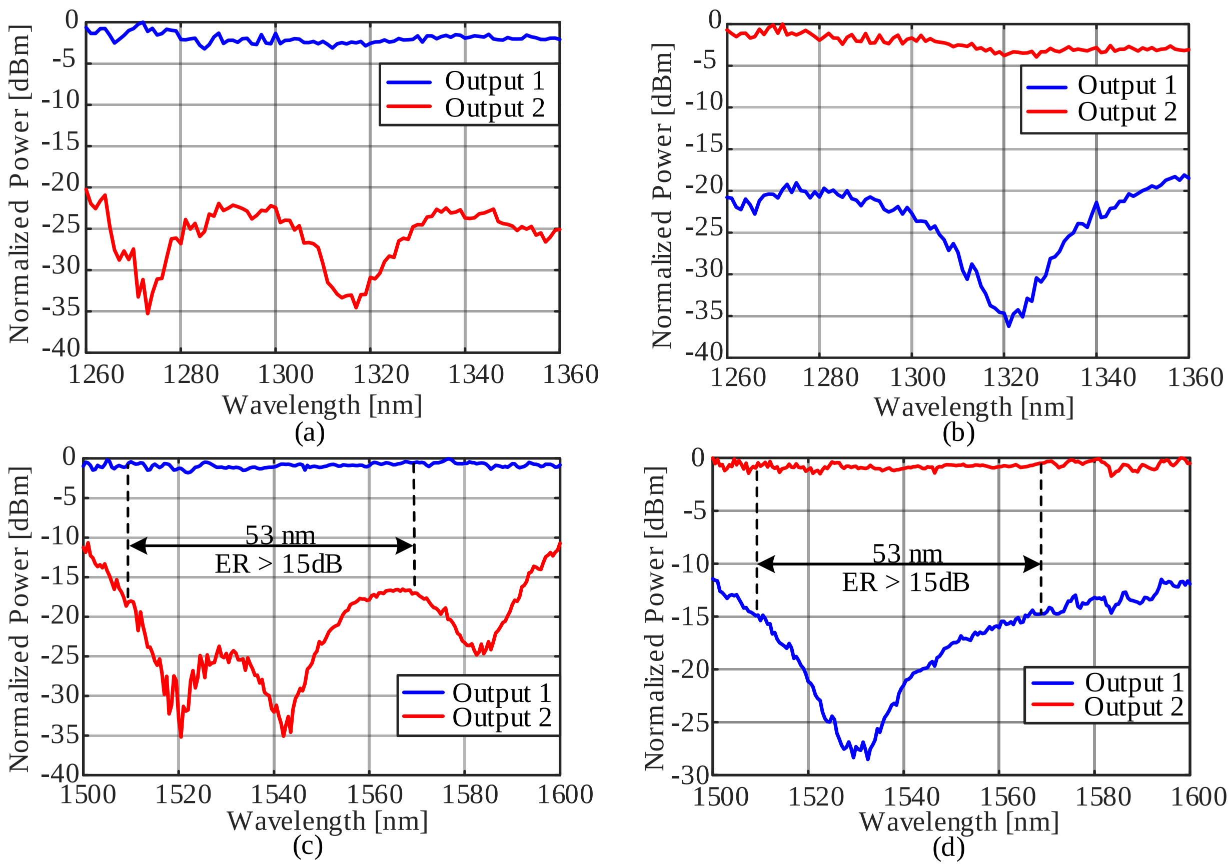

Figure 18. Normalized output power at the two switch output ports versus wavelength for (a) Bar state in O-band. (b) Cross state in O-band. (c) Bar state 1500-1600nm range. (d) Cross state in 1500-1600nm range.

Figure 18(a) and (b) show the switch operation over the O-band in the bar and cross state, respectively. An extinction of at least 15 dB is achieved over the entire O-band. Similarly, Figure 18(c) and (d) show the switch operation in the 1500 -1600 nm wavelength range in the bar and cross states, respectively. An extinction of at least 15 dB is achieved over 53 nm which include the entire C- band. It is also noteworthy that we were not able to test the entire simulation bandwidth (from 1200-1600 nm inclusively) due to the unavailability of a sufficiently broadband laser capable of covering the entire wavelength range of the switch. However, we believe that the switch should also operate in the untested wavelength range that covers the E and S- bands.

Moreover, we performed small signal and large signal analysis to characterize the heater used in order to determine the switching speed of our designed switch. The setup that was used is shown in Figure 19. An output of an Agilent 33500B waveform generator (WG) was applied to the heater via a DC probe while the other output was used as a reference and fed directly into one channel of a 5 GSa/s Tektronix TDS 684B Oscilloscope having 1 GHz analog bandwidth. Unmodulated CW light from a tunable laser was coupled into input port 1 of the switch using the fiber array and the output signal was detected by a 40 GHz PIN/TIA and viewed on the scope.

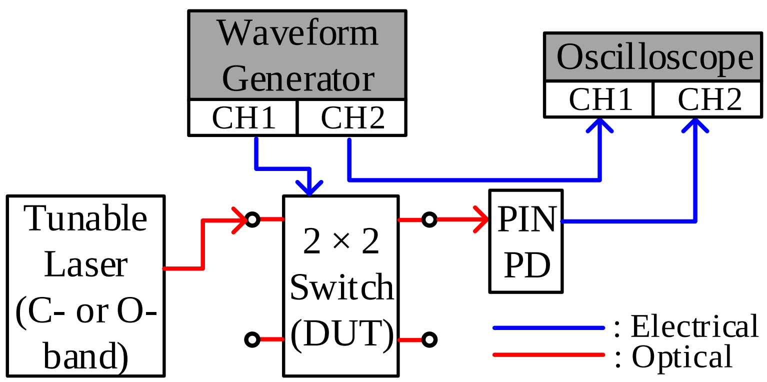

Figure 19. Experimental setup for heater characterization and switching time measurements

First, small signal analysis was performed on the thermo-optic phase shifter to determine its frequency response. A sinusoidal signal with a small amplitude of 0.2 V_{pp} was generated from the WG and applied on the heater. The frequency of the sinusoidal signal was swept, and the output of the switch after being passed on the PD was recorded. The small voltage swing of the heater input was chosen to guarantee linear mapping of the applied sinusoidal voltage into a sinusoidal optical output from the switch. The measured frequency response of the heater is shown in Figure 20(a), where the 3 dB bandwidth of the heater was found to be 22.5 KHz. It should be noted that this measured frequency response also includes the response of the DC probe along with that of the thermo-optic phase shifter. The remaining frequency responses of the PIN/TIA, WG and oscilloscope are also present but they are all broadband enough to be assumed transparent with respect to the bandwidth of heater.

Finally, we performed large signal analysis on the thermo-optic phase shifter to measure the switching time of our 2×2 switch; which is the time required to switch between the bar and cross operating states of the switch. We generated a square wave with a peak-to-peak voltage swing of 0.43 V and a DC offset of 1.44 V. The peak-to-peak voltage and DC offset were carefully chosen to ensure proper switching between bar and cross states in order to measure the required switching time. The output from the switch and the reference signal from the WG were monitored on the scope. A screenshot from the scope is shown in Figure 20(b) viewing time domain waveforms of both the output from the switch (top) and the reference square wave applied to the heater (bottom) when the frequency of the square wave was set to 15 kHz. The 10% – 90% switching times were found to be 8.4 µs (rise) and 13 µs (fall) as depicted on the waveform in Figure 20(b). Switching time can be dramatically decreased by using other phase-shifting approaches such as the electro-optic effect (carrier depletion).

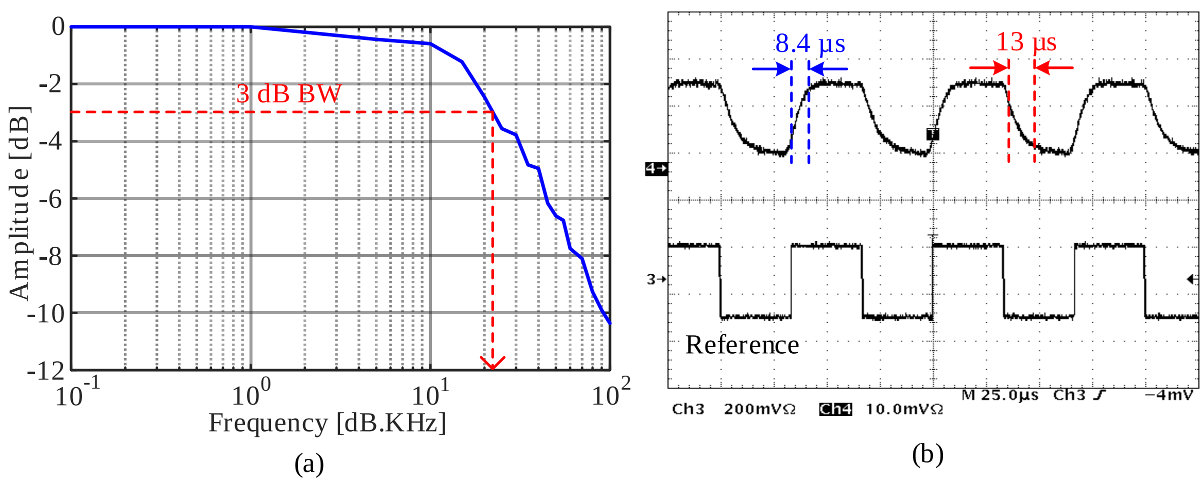

Figure 20. (a) Heater frequency response showing 3 dB bandwidth. (b) Switch response (top) to an applied square electrical signal (bottom) on heater.

3.5.2 Live traffic experiment

In this section, we study the effect of the finite switch extinction ratio in the presence of crosstalk on the BER when the switch is placed in a full transmission system and live data is transmitted. Figure 21 shows the experimental setup used for this part of the experiment.

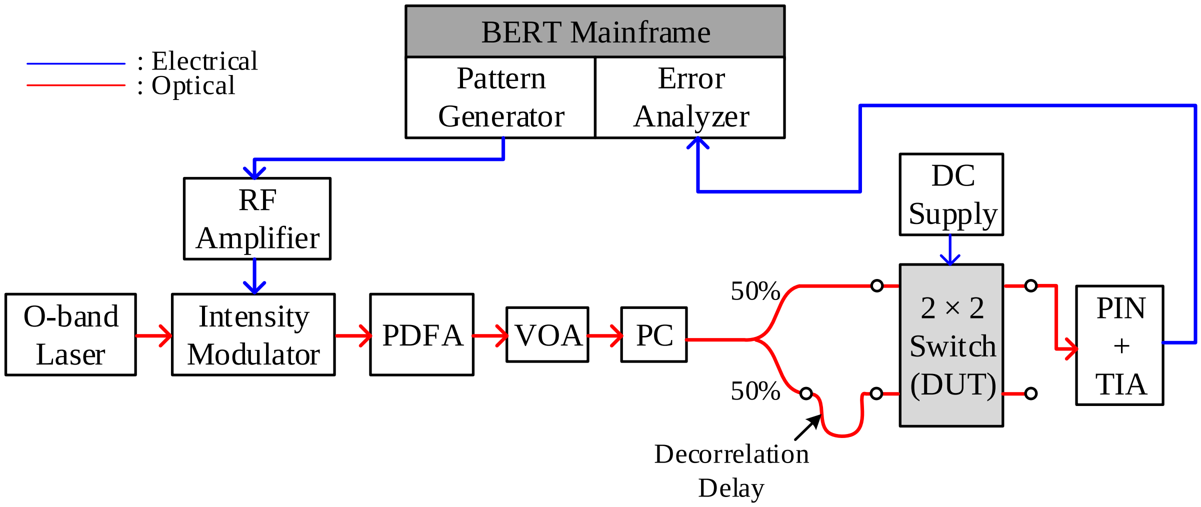

Figure 21. Experimental setup for live traffic experiment.

A pulse pattern generator (PPG) was used to generate a pseudo-random binary sequence (PRBS-31), which was first amplified using a 38 GHz RF amplifier. The amplified signal was driven by a 30 GHz $LiNbO_3$ Mach-Zehnder intensity modulator which was fed from a 1310 nm CW laser. Next, a Praseodymium doped fiber amplifier (PDFA) was used to optically amplify the OOK modulated data. A variable optical attenuator (VOA) was used to sweep the signal power. In order to maximize the coupling into the chip, a polarization controller (PC) was used to align the polarization of the signal to the fundamental TE mode prior to coupling light into the chip. The signal was equally split using a polarization maintaining (PM) 3 dB power splitter. One splitter output was injected into input port 1 of the switch, the second output was connected to a PM patch cord to de-correlate the data between the two branches before being fed into input port 2 which will act as the "undesired" interfering data. The patch cord was 1 m long which guaranteed sufficiently decorrelated data streams at both input ports of the switch, (~140 and 244 bits of decorrelation delay at 28 and 50 Gb/s, respectively). The transmitted data was then detected using a 47 GHz PIN/TIA followed by an error analyzer (EA). Measurements were done at an applied voltage of 0.68V on the heater, which corresponded to bar operation state of the switch. Using the VOA, the received optical power at the input of the PIN/TIA was varied and BER was recorded from the EA at two data rates of 28 and 50 Gb/s in two scenarios: (i) in the presence of interference from the second input port, and (ii) in the absence of interference from the second input port.

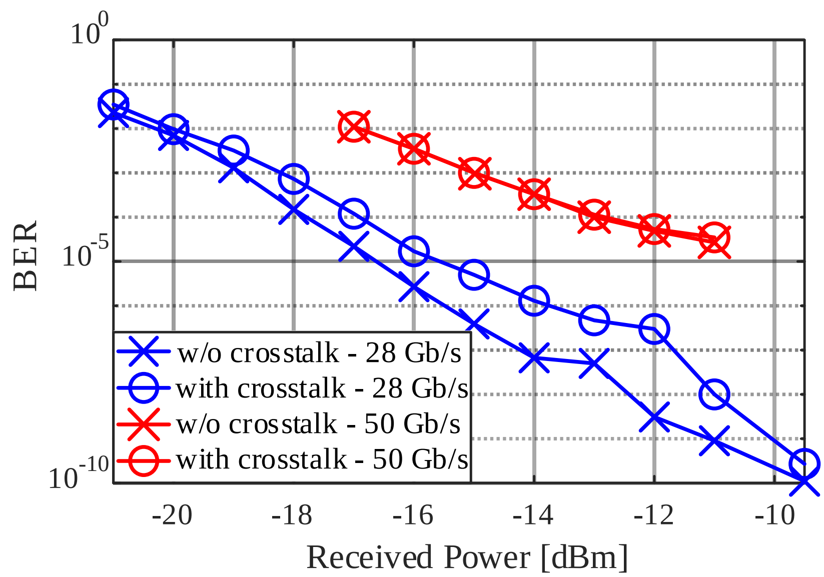

Figure 22. Experimental results showing BER versus received power at 28 Gb/s and 50 Gb/s with and without interference from the second input port.

Figure 22 shows the BER versus received power at both 28 and 50 Gb/s in the presence and absence of interference from the second "undesired" input port. At 28 Gb/s we can observe the impact of the presence of the interfering signal from the second input port of the switch on the BER, especially as the received signal power increases. This is due to the fact that at lower received powers, the performance was limited by the stronger effect of receiver noise rather than the crosstalk. On the other hand, at 50 Gb/s the impact of the crosstalk was minimal for all received signal powers. This is because the performance at such high bit rate was not limited by the interference but rather, by the quality of the electrical transmitted signal generated by the PPG and the RF amplifier. These observations lead to the conclusion that the extinction ratio of the switch was sufficient to ensure proper operation at either bit rate in presence of the interfering signal at the second input port of the switch.

3.6 Conclusion

In this chapter, we used the proposed design for a broadband AC as a building block for an ultra-broadband 2×2 switch that operates simultaneously over the O- and C- bands for different applications. The switch design was also simulated and showed an extinction ratio of at least 15 dB between both ports of the switch. The switch was fabricated using EBL and was fully characterized experimentally in terms of bandwidth, extinction ratio and switching time. Experimental measurements showed an extinction ratio of at least 15 dB achieved over the entire O-band and over 53 nm (in the wavelength range 1500-1600 nm) which include the entire C- band, yielding a total experimentally verified operational bandwidth of 153 nm. The 10% - 90% switching times were also found to be 8.4 µs (rise) and 13 µs (fall). Furthermore, we used the designed and fabricated switch in a live traffic setup in order to study the effect of crosstalk from the "unused" switch port on the BER performance. OOK-modulated data was transmitted at rates of 28 Gb/s and 50 Gb/s on input port(s) of the switch, the output BER was recorded in two scenarios; with and without the presence of interference from the second "unused" input port of the switch. At the data rate of 28 Gb/s, an SNR penalty of ~ 1 dB was seen due to the crosstalk from the second input port, while when transmitting at a rate of 50 Gb/s there was no crosstalk penalty since the performance at the higher rate is limited by the electrical signal quality and not crosstalk.

Chapter Four

Waveguide Bragg Gratings

Bragg gratings are "wavelength selective" photonic devices. Murphy et al. [42] first introduced SOI integrated Bragg gratings in 2001 and ever since numerous research efforts has yielded various grating structures that are widely used in multiple applications.

In this chapter we will review the basic concepts of uniform Bragg gratings followed by their key design parameters and design process flow. Next, we will explain how their simulation procedure works and explore briefly other types of gratings. Finally, we mention some of the applications where Bragg gratings are used.

4.1 Background

Waveguide Bragg gratings are photonic band-structures whose effective refractive index is periodically modulated along the direction of propagation. This can be achieved by alternating the material periodically or by changing the physical dimensions of the structure. The index modulation results in a series of reflections at each boundary. The accumulated phase (of the reflection) at each boundary depends on the grating period and the incident light wavelength. Depending on the phase of these reflections, they will either interfere constructively or destructively. At a certain wavelength range (around Bragg wavelength), the reflections will interfere constructively and will hence add up and this wavelength will be totally reflected (i.e. Bragg grating acts as a mirror for this wavelength). The Bragg wavelength satisfies the condition:

$$\lambda_B = 2\, n_{eff} \Lambda \tag{1}$$

known as the Bragg condition, where λ_B is the Bragg wavelength, n_{eff} is the effective index of the waveguide and Λ is the grating period. As the number of grating periods increases, the reflection strength will increase and we can achieve a near unity reflection, however the propagation losses will increase subsequently.

Due to the structure and periodicity of the grating, rigorous application of Maxwell's equations is not possible. Hence, coupled mode theory is conventionally used for theoretical analysis of such devices.

Below are the key governing equations that relate the Bragg grating parameters such as the reflection coefficient, bandwidth and coupling coefficient which are the result of coupled mode theory analysis of gratings. The full derivations of all the equations can be found in [43].

$$r = \frac{-i\kappa \sinh(\gamma L)}{\gamma \cosh(\gamma L) + i\Delta\beta \sinh(\gamma L)} \tag{2}$$

where (r) is the grating reflection coefficient, (κ) is the grating coupling coefficient whose expression depends on the index of modulation of the grating (i.e. step index, sinusoidal, etc.) and can be interpreted as the number of reflections per unit length, (L) is the grating length, (Δβ) is the propagation constant detuning from the Bragg wavelength and (γ) is given by the following equation:

$$\gamma^2 = \kappa^2 - \Delta\beta^2 \tag{3}$$

The propagation constant detuning (Δβ) is related to the group velocity (n_g) and the grating bandwidth (Δλ) through the following equation:

$$\Delta\beta = \beta - \Delta\beta_o = \frac{2\pi n_{eff}(\lambda)}{\lambda} - \frac{2\pi n_{eff}(\lambda_B)}{\lambda_B} \approx -\frac{2\pi n_g}{{\lambda_B}^2}\Delta\lambda \tag{4}$$

where the group index (n_g) appears in Eq. (4) due to the wavelength dependence of (n_{eff}) as per the equation below, this dependence plays an important role in the group delay response of the grating which can be used for dispersion compensation as we will discuss later:

$$n_g = n_{eff} - \lambda \frac{dn_{eff}}{d\lambda} \tag{5}$$

The peak reflection at the Bragg wavelength can be found by substituting $\Delta\beta = 0$ in Eq. (2) yielding:

$$r = -i \tanh(\kappa L) \tag{6}$$

It is clear from Eq. (6) that the peak reflection depends on the coupling coefficient and the length of the grating, which is expected since a large coupling coefficient (κ) means a higher number of reflections per unit length and as the length of the grating increases, the reflections will also increase. The peak power reflectivity at the Bragg wavelength is given by:

$$R_{peak} = tanh^2(\kappa L) \tag{7}$$

The bandwidth of the grating (Δλ) is a very important parameter since it determines the wavelength range that will be reflected (stop band), it refers to the bandwidth between the first two nulls around the reflection peak not the 3-dB bandwidth of the grating. It is noteworthy that at each reflection a phase of π/2 is accumulated. The term $\sqrt{\Delta\beta^2 - \kappa^2}$ determines whether the incident wavelength will be reflected (exponentially decaying wave where $\Delta\beta < \kappa$) or transmitted (wave with propagation constant = $\sqrt{\Delta\beta^2 - \kappa^2}$). The bandwidth for a lossless grating is given by the expression:

$$\Delta\lambda = \frac{{\lambda_B}^2}{\pi n_g}\sqrt{\kappa^2 + \left(\frac{\pi}{L}\right)^2} \tag{8}$$

As discussed earlier, the operation principle of Bragg gratings is refractive index modulation along the direction of propagation. Bragg gratings fabrication in optical fibers rely on the photosensitivity of the fiber core, where it exposed to intense UV radiation that results in refractive index modulation in the fiber core. On the other hand, Bragg gratings in SOI platform are fabricated by modulating the effective index of the waveguides through sidewall corrugations that are inscribed in the waveguide using deep Ultraviolet lithography or electron beam lithography. Our focus here is on SOI Bragg gratings for TE modes.

There are different types of gratings that include uniform gratings, chirped gratings, phase-shifted gratings and sampled gratings that were fabricated on strip or rib waveguides. Each grating structure was driven by a specific application and exhibits a specific advantage, in the following sections we will discuss some of these grating structures.

4.2 Uniform Bragg Gratings

Uniform Bragg gratings are the most common type of gratings that are widely used in photonic applications. They have a constant grating period that does not change over the entire grating length hence they are simpler to design and play an important role in various applications such as in Optical add and drop multiplexers (OADMs) for WDM applications [16]. SiP Uniform gratings can be realized on strip waveguides or rib waveguides as will be explained later in subsection 4.2.1. In this section, we will discuss the design process of Uniform Bragg gratings on strip and rib waveguides along with the simulation procedure.

4.2.1 Design

The design process flow that was proposed in [44] was used for waveguide Bragg grating design. We begin by choosing the waveguide width. Conventionally, a waveguide width of 500nm is used for single mode operation in the C-band and smaller width for single mode operation in the O-band. As for the waveguide thickness, we mentioned before in section 1.1.3 that the waveguide thickness for SiP devices has been set to be 220 nm by the foundries for MPW runs. Next, we used Lumerical Mode Eigenmode solver for simulation of the waveguide of the chosen width in order to extract the effective index. The extracted effective index from the simulations is then plugged into Eq. (1) which is the Bragg condition equation to find the grating period for operation at the desired wavelength of operation. Finally, the corrugation depth can be varied in simulations until we obtain the desired bandwidth of operation. The sidewall corrugations will vary the waveguide structure and hence change the effective index over the grating period. The corrugation depth (Δw) can be either recessed into the waveguide or protruding, but in order to maintain the average effective index constant it is preferable to have a series of corrugations of depth $W \pm \Delta w/2$. Figure 23 shows the design of a typical uniform waveguide grating with a waveguide width (W).

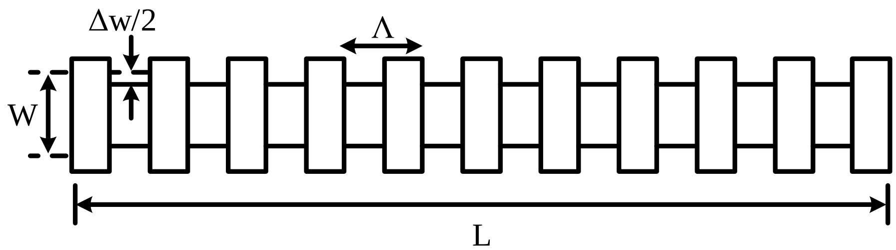

Figure 23. Design of a typical uniform waveguide Bragg grating. W: waveguide width, Δw: corrugation depth, Λ: grating period and L: grating length.

Another important factor that needs to be considered in waveguide Bragg gratings design are the lithography effects since the fabrication of commercial silicon photonic devices require a step of deep ultraviolet (DUV) lithography. Hence, lithography effects should be taken into account during design and simulations as we will further explain in the following sections.

4.2.1.1 Strip waveguides

Strip waveguides are the most commonly used waveguides. The mode is confined in the center of the waveguide and thus they are used for on chip routing and for bends since their bending losses are significantly less than other waveguide structures [3]. Thus, strip waveguides dimensions are typically in the submicron level and Bragg gratings are fabricated by introducing periodic corrugations in the sidewalls of the waveguide. Consequently, due to their small size and mode confinement in the center of the waveguides, the sidewall corrugations will cause large mode perturbations and induce a large grating coupling coefficient which is the reason behind the large bandwidth of gratings on strip waveguides (relative to their rib counterparts). Figure 24 shows the TE mode profile in a strip waveguide of 500 nm width with oxide cladding and a 3-D drawing of a uniform grating on a strip waveguide. If a smaller bandwidth is required, the sidewall corrugations need to be very small which is not always feasible due to fabrication constraints. Another approach to decrease the grating bandwidth is to use rib waveguides to realize narrow band Bragg gratings as we will discuss in the next section.

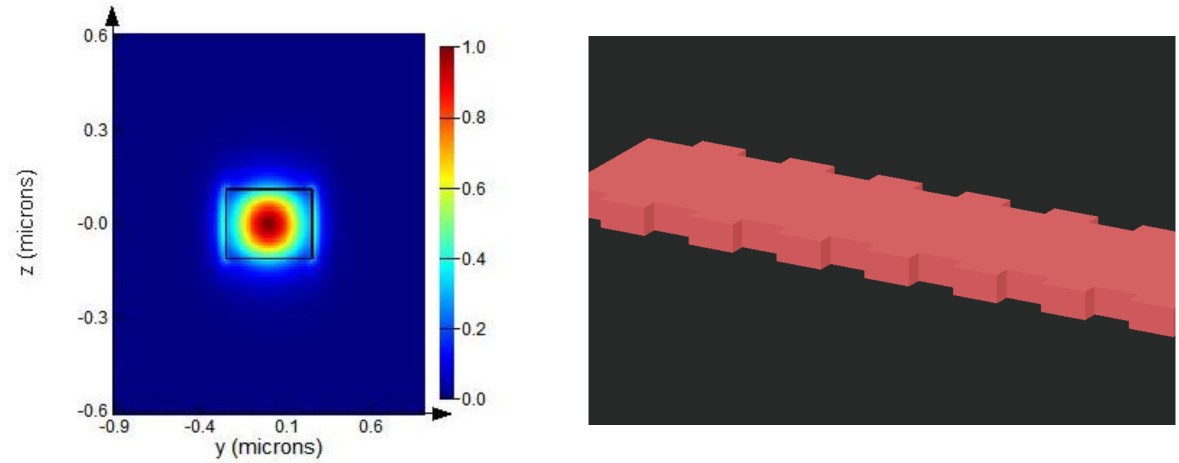

(a) (b)

Figure 24. (a) TE mode in a 500 nm wide strip waveguide with oxide cladding showing mode confinement in the center of the waveguide. (b) 3D view of a typical strip waveguide Bragg grating.

4.2.1.2 Rib waveguides

Rib waveguides consist of a narrow rib on top of an infinite slab. Due to the structure of the rib waveguide, it allows more than one grating design i.e. the grating corrugations can be in the rib or the slab [45]. Figure 25 shows the structure of a typical rib waveguide and the TE mode profile in a rib waveguide with a 1 µm and 500 nm slab and rib widths, respectively. It is clear that the mode is mainly confined under the rib and rib waveguides typically have larger dimensions than strip waveguides. Although they are typically designed for single mode operation, due to the large size of the slab the risk of excitation of higher order modes is higher here than the case of strip waveguides and power in the fundamental TE mode might be lost into other modes.

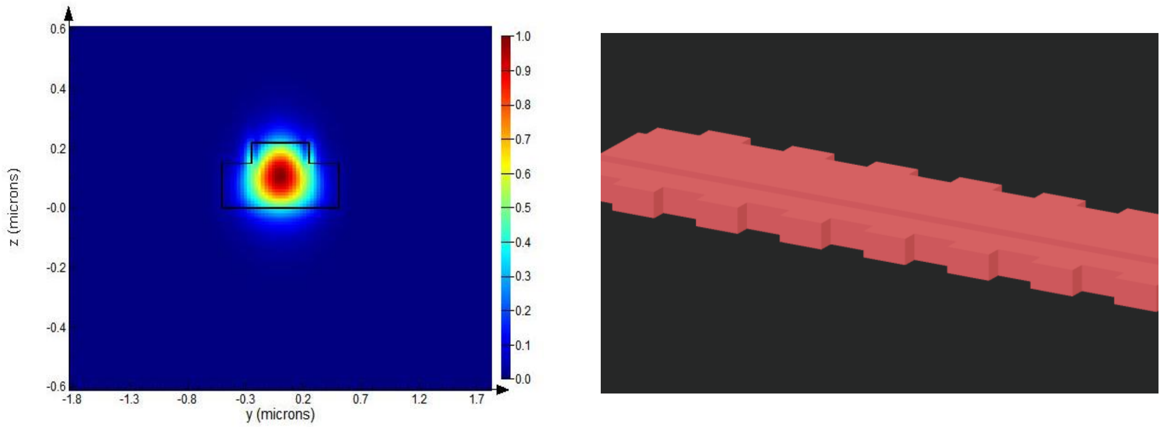

(a) (b)

Figure 25. (a) TE mode in a rib waveguide with slab width of 1 µm and 500 nm rib width showing the mode confinement under the rib. (b) 3D view of a rib waveguide Bragg grating.

On the other hand, since the mode is confined mainly under the rib, the interaction between the mode and the sidewall corrugations is less than in the case of strip waveguides which lead to a smaller grating coefficient in the case of rib gratings. Hence, a narrow grating bandwidth is feasible using rib waveguides which is suitable for WDM applications as we will explain in section 4.4.1. Moreover, their larger dimensions make them more fabrication tolerant than their strip waveguide-based counterparts [3].

4.2.2 Simulation

Waveguide Bragg gratings are usually a few hundred of microns long, which means that it is a relatively long device and simulating such a device efficiently is not straightforward. FDTD simulations allow us to predict the fabricated device performance as accurate as possible. However, a very fine mesh is required for simulating such a device that has corrugation depths in the order of nanometers to enable resolving these small sidewall field interactions. Moreover, the used mesh cells must align perfectly with the corrugations of the grating in order to eliminate errors thus a mesh override is used to force the mesh points to be an integer multiple of the grating period. Hence, a long Bragg grating will require an unreasonable number of simulation hours as well as enormous memory requirements. In [46], an efficient method was proposed to use FDTD to accurately identify the bandwidth ($\Delta\lambda$) and the Bragg wavelength (λ_B) of the grating design. A single unit cell of the grating which consists of the recessed and protruding part of the waveguide i.e. a full grating period is used and we assume an infinitely long grating structure. Bloch boundary conditions are applied along the direction of propagation, and the Bloch wave number (kx) is set to be (π/Λ) in order to identify the bandgap of the Bragg grating. Bloch boundaries feed the output power from one boundary into the other, hence it forms a loop on the single unit cell for the entire simulation time. Furthermore, the simulation can be done more efficiently and the simulation time can be scaled down by a factor of 2 by using the Anti-symmetric boundary conditions to make use of the grating symmetry along the y-axis. Frequency domain power monitors can be used to capture the transmitted power and identify the bandgap or the band-structure analysis group which is built in FDTD to find the resonant frequencies of photonic structures. Once the bandwidth and the Bragg wavelength are identified, the coupling coefficient (κ) can be calculated from Eq. (8), and the required grating length can be found from Eq. (7). A full simulation of the entire length of the device using FDTD is not feasible (especially for very long gratings of periods > 500), since such a simulation will have huge memory requirements and will terminate immaturely. Also, we are unable to exploit the periodicity of Bragg grating structures and use Bloch boundaries to simulate the full device and run wavelength sweeps to capture the transmission and reflection spectra, because the power monitors will accumulate the power passing through it after each grating period and will not give correct results. We tried to use time apodization in the monitors to enable capturing only a part of the field at a specific time, but the results were also inaccurate. We reproduced the results in [46] using the aforementioned method to find the grating wavelength and bandwidth, the simulation results are shown in Figure 26. As seen in the figure, the Bragg wavelength is around 1545 nm and the bandwidth is ~ 20 nm which agree with the results published in the paper.

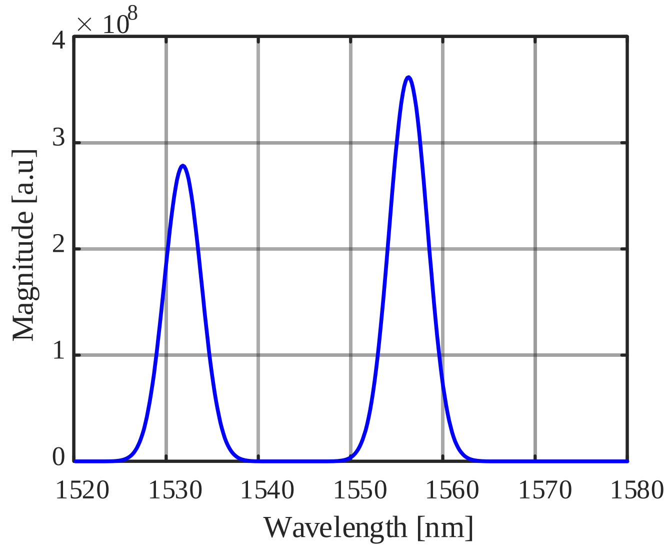

Figure 26. Band-structure simulation of Bragg grating with air cladding, Λ = 324 nm, W = 500 nm, Δw = 50 nm and ΔL = 0 (no misalignment).

Also, since the grating in the paper had 284 grating periods (the grating length is about 92 µm so it is not extremely long), we performed full device simulations using FDTD and recorded the transmission and reflection spectra of the grating. Our FDTD simulations are shown in Figure 27, which agree with the experimental transmission and reflection spectra measurements in the paper. It is expected that the results from band-structure analysis and full device simulation using FDTD will not perfectly match because the aforementioned band-structure analysis (results shown in Figure 26) is only valid for infinitely long gratings. We noted a few things during simulating the device using FDTD, if the mesh size is not fine enough and perfectly aligned to the sidewall corrugations, the results are not accurate and the center wavelength shifts dramatically. In other words, mesh size and aligning the mesh correctly to the grating periods are crucial to obtain correct simulations that will actually predict the performance of the fabricated device experimentally.

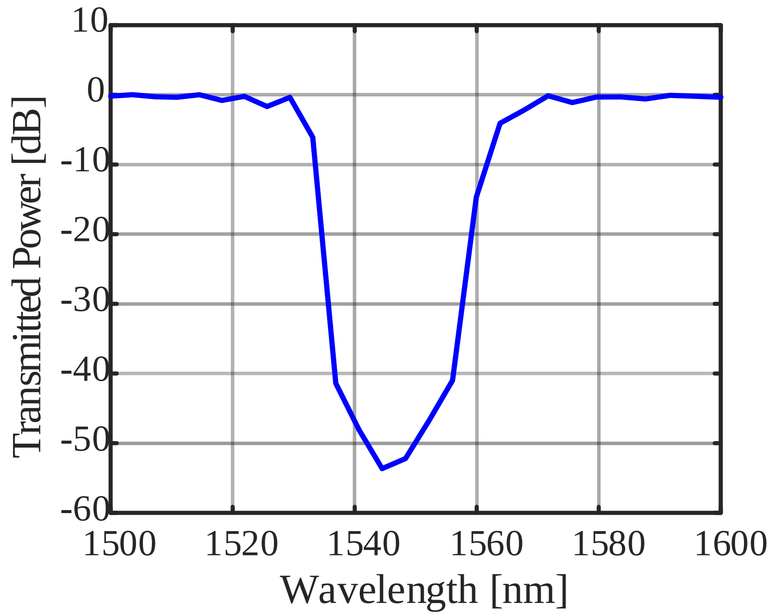

Figure 27. Simulated transmission spectrum of uniform Bragg grating in [46] using FDTD with air cladding, Λ = 324 nm, W = 500 nm, Δw = 50 nm and ΔL = 0 (no misalignment).

On the other hand, full device simulations can be done efficiently using Lumerical Mode Eigen Mode Expansion (EME) solver, which although not as accurate as FDTD it provides a good prediction of the performance of the device. EME enables very efficient simulations of very long devices by exploiting their periodic nature. First, we define the grating period as a group that consists of two cells, each has a different waveguide width (W ± ΔW/2). Next, the group is simulated N-times, where N indicates the number of grating periods and is equal to (N = L / Λ) and the s-parameters can be extracted easily. However, this simulation is done at a single wavelength hence a large number of simulations is needed to cover the entire spectrum and the modes tend to be discontinuous which may lead to errors at the boundaries. This is the reason why in most publications, the simulations done do not include wavelength sweeps. The transmission and reflection spectra of the gratings are measured experimentally in the lab due to the tedious simulation time and memory required to simulate these long devices at each wavelength in order to cover the required bandwidth of interest.

Another approach for simulating Bragg gratings is using the compact model (CML) provided in the process design kit (PDK). This CML can be imported in softwares such as Lumerical Interconnect and allow some parameter variations such as adjusting the grating period, corrugation depth, length, etc. This method allows circuit-level simulation of the grating with the possibility of adjusting the aforementioned parameters to tailor the desired center wavelength and bandwidth. However, the possible parameter variations are limited, and only compact models of uniform Bragg gratings are available.

It is noteworthy that lithography effects were not considered in all the simulation procedures discussed above. The lithography step in the fabrication process causes rounding of squared edges, hence the designed rectangular sidewall corrugations tend to be sinusoidal after fabrication. Figure 28 shows a fabricated Bragg grating where the corrugations after fabrication are sinusoidal not rectangular. These sinusoidal corrugations will affect the mode interaction with the sidewalls and change the effective index of the waveguide, hence it will affect the grating coupling coefficient which in return will shift the Bragg wavelength of the fabricated grating and alter its bandwidth. Therefore, it is crucial to include the effect of lithography while simulating Bragg gratings in order to be able to accurately predict its performance after fabrication. More information on including lithography effects in simulations are thoroughly explained in [47].

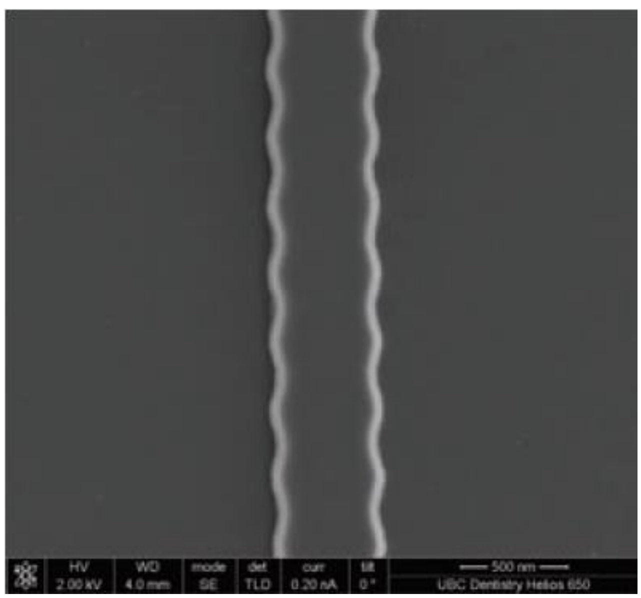

Figure 28. Fabricated waveguide Bragg grating showing the effect of lithography on the rounding of sidewall corrugations. Figure excerpted from [3].

4.3 Other grating types

As discussed in section 4.2, the most well known and common Bragg gratings are the uniform Bragg gratings whether on strip or rib waveguides. However, there are other more complex grating structures that were published over the years that target different applications by manipulating the various grating parameters.

In this section, we briefly mention other types of gratings that have more complex structures and different design parameters highlighting the key applications where each grating type is used.

4.3.1 Chirped (non-uniform) gratings

Non-uniform waveguide Bragg gratings as the name suggests have a non-uniform grating period that varies along the direction of propagation. Figure 29 shows the design of a linearly chirped grating and the difference between uniform and non-uniform gratings in terms of grating period variation along the grating length. Grating period variation induces a change in the effective index which results in a change in the group index of the grating as per Eq. (5). This is useful to tailor the group velocity of the input signal to oppose dispersion effects. Depending on whether the grating period increases or decreases along the direction of propagation the grating is either positively or negatively chirped. For example, positively chirped gratings with grating period increasing along the direction of propagation will reflect shorter wavelengths first and then longer ones after a series of reflections. Thus, longer wavelengths will propagate longer in the waveguide grating and hence are delayed more than the shorter ones which opposes the accumulated delay in the fiber and compensate for dispersion. We will discuss the role of Bragg gratings in optical dispersion compensation in the next section.

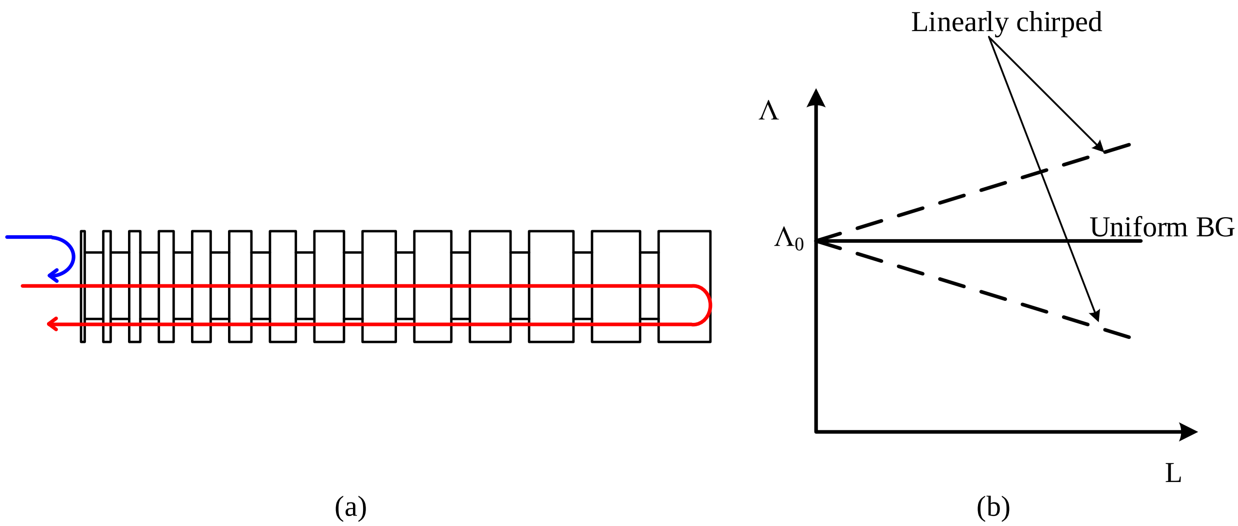

Figure 29. (a) Structure of a linearly chirped Bragg grating where blue (short) wavelengths are reflected first at the beginning of the grating followed by the red (long) wavelengths at the end of the grating hence red wavelengths are delayed relative to the blue wavelengths, (b) Graph showing the variation of grating period over the grating length for linearly chirped and uniform Bragg gratings.

4.3.2 Phase shifted gratings

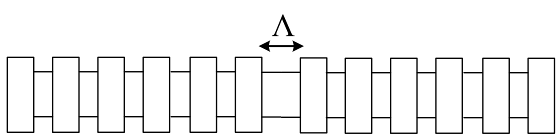

Figure 30. Design of a strip phase-shifted waveguide Bragg grating. A Λ phase shift is introduced in the middle of the grating.

Figure 30 shows the design of a phase shifted grating on a strip waveguide. Phase shifted gratings are uniform Bragg gratings where a phase shift is introduced within the grating length. Introducing this phase shift causes the appearance of a narrow resonant transmission frequency in the reflection spectrum of the grating i.e. a narrow passband is introduced within the grating stop-band. The length and position of the phase shift determines the sharpness as well as the wavelength of the transmission window. This is useful in filtering applications such as the Hilbert transformer [48] and in distributed feedback (DFB) lasers to eliminate the mode degeneracy and increase the mode stability [49].

4.3.3 Sampled gratings

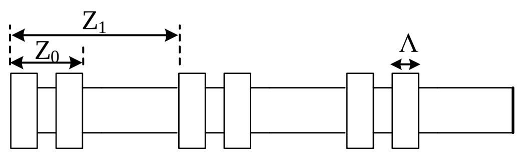

Figure 31. Design of a sampled waveguide Bragg grating. Z_0: burst period, Z_1; burst length, Λ: grating period.

Sampled gratings are basically the result of multiplying a uniform grating by a sampling function, as shown in Figure 31. The sampling function causes a series of periodic maxima in the spectrum, thus our overall spectrum is the result of convolving the periodic maxima with the grating reflection spectrum. This yields several periodic narrow-band reflections which are useful for tunability of the bandwidth. Apart from the grating period and corrugation depth, the most important parameters in sampled gratings are the burst length (Z_1) and burst period (Z_0). The ratio between Z_0 and Z_1 determines the number of peaks within the 3-db bandwidth of the grating. The full theory of sampled gratings is explained in [50]. They have been fabricated on optical fiber and used in dispersion compensation of 51 WDM channels that are 100 GHz spaced as in [51] and for extending the tunability range of semiconductor lasers as in [50]. Recently, sampled gratings were demonstrated and fabricated on SOI as published in [52] where they mention some potential applications for SiP sampled gratings such as in tunable silicon lasers and biosensors.

4.4 Applications of Bragg gratings

4.4.1 Bragg gratings as wavelength selective filters

For WDM applications (100 GHz or 0.8 nm channels) in which a very narrow bandwidth is required for filtering/multiplexing/demultiplexing the densely spaced channels, rib waveguide Bragg gratings are suitable for this application. A demonstration of 20 reflection channels that are 0.78 nm spaced realized using a sampled Bragg grating on a rib waveguide with an insertion loss less than 1 dB, which is suitable for 100 GHz WDM networks was published in [53]. Furthermore, very narrow band gratings were also fabricated on SOI with CMOS compatible process using rib Bragg gratings with a channel spacing of 0.4 nm that is suitable for 50 GHz WDM networks [45].

OADMs are also a very important device in WDM systems to add or drop certain channels (wavelengths) along the transmission link. A single stage OADM using misaligned waveguide Bragg gratings with a 3 dB bandwidth of 6 nm and extinction of 25 dB was demonstrated in [16]. The cascaded design has provided a 51 dB extinction at the expense of a larger footprint.

Wavelength/frequency selectivity of Bragg gratings and their tunability has made gratings widely used in sensing applications. Integrated Bragg grating sensors on SOI were fabricated for temperature sensing [54] and biosensing [55].

4.4.2 Bragg gratings for optical dispersion compensation (ODC)

Propagation in the optical fiber induces positive dispersion (broadening of the pulse) where wavelengths travel faster than the ones. Since chirped gratings exhibit negative group velocity dispersion, they were used to induce a negative dispersion to oppose the fiber dispersion and compensate for it. Fiber Bragg gratings have been used for chromatic dispersion compensation optically over two decades ago and allowed high speed transmission over hundreds of kilometers. The wok published in [56] is among the most notable fiber Bragg grating ODC, where they were able to compensate dispersion over multiple WDM channels after propagating for 240 kms using a12 cm long chirped grating. Similarly, integrating ODCs on chip to compensate for the accumulated dispersion from fibers connecting different chips was proposed in [57] where they introduced the non-uniformity using a tapered structure on a rib waveguide. Also, in [58] the authors demonstrate dispersion values of up to 8.4×10^{5} ps/nm/km using coupled chirped Bragg gratings.

4.5 Conclusion

In this chapter, we provided an overview on SiP based waveguide Bragg Gratings. We reviewed various grating structures and how such long devices can be efficiently simulated. We finally performed simulations on a uniform Bragg grating to evaluate the effect of varying grating parameters as well as mesh settings in the simulation tools on predicting the Bragg wavelength and operating bandwidth. Finally, we summarized some of the applications in which Bragg gratings are used.

Chapter Five

Conclusion

Silicon Photonics is a promising platform that enabled integration of hundreds of devices on a single chip. Its compatibility with the mature CMOS technology made SiP devices very appealing for high volume, low cost production of photonic devices which are used in optical communications, medical sensing and other applications.

The ever-growing capacity demand has driven the demand for utilizing other operating wavelength windows (or bands) such as the O- and L- bands beside the C-band that is conventionally used for metro / long-haul optical communications. This drives the demand for designing efficient broadband devices that operate colorlessly across multiple wavelength bands. Ultra-broadband SiP devices that are transparent to the wavelength of operation is a subject of intensive research and development including passive devices (e.g. couplers, switches, polarization splitters, etc.) and active devices (e.g. modulators, detectors, etc.). In this thesis, the design, simulations and testing of an ultra-broadband adiabatic coupler and a 2×2 ultra-broadband adiabatic coupler-based switch were presented along with theoretical analysis of waveguide Bragg gratings and their simulations.

In chapter 2, an ultra-broadband 3 dB adiabatic coupler on SOI with an overall experimentally verified optical operating bandwidth of at least 160 nm is presented. The splitting ratio of the coupler is 3±0.3 dB and 3±0.8 dB over the wavelength range 1500 to 1580 nm and 1280 to 1360 nm, respectively. The total device footprint is 100 µm × 2.5 µm. The experimental results are in good agreement with our simulations and the design is CMOS compatible. Our work on the adiabatic coupler has been published in [21].

In chapter three, we used the aforementioned adiabatic coupler to fabricate an ultra-broadband 2x2 switch with a thermo-optic phase shifter to control the switch operation. The proposed switch exhibits an extinction of at least 15 dB over the entire O-band and over the wavelength range 1515 to 1568 nm (which includes the entire C-band), i.e. an overall optical operating bandwidth of 153 nm over which the extinction between both ports is at least 15 dB. The switching speed was found to be 13 µs and the electrical power consumption was 29 mW. Furthermore, we studied the effect of crosstalk on the BER due to the finite extinction of the switch by transmitting OOK data at 28 and 50 Gb/s.

We finally studied the operating principle of waveguide Bragg gratings, explored different grating structures along with the applications to which they are suited. Next, we discussed the methodology of grating design. We also studied how simulating such long devices efficiently can be performed. We simulated a uniform Bragg grating to study the effect of varying the grating parameters on its Bragg wavelength (center wavelength) and operating bandwidth. Some applications for Bragg gratings were also discussed.

References

[1] G. T. R. a. A. P. Knights, *Silicon Photonics: the state of the art*. Wiley, 2008.

[2] R. Soref, "The Past, Present, and Future of Silicon Photonics," *IEEE Journal of Selected Topics in Quantum Electronics,* vol. 12, no. 6, pp. 1678-1687, 2006.

[3] L. C. a. M. Hochberg, *Silicon Photonics Design*. Cambridge University Press, 2015.

[4] A. H. Atabaki *et al.*, "Integrating photonics with silicon nanoelectronics for the next generation of systems on a chip," *Nature,* vol. 556, no. 7701, pp. 349-354, 2018/04/01 2018.

[5] R. Soref and B. Bennett, "Electrooptical effects in silicon," *IEEE Journal of Quantum Electronics,* vol. 23, no. 1, pp. 123-129, 1987.

[6] J. Sun, R. Kumar, M. Sakib, J. B. Driscoll, H. Jayatilleka, and H. Rong, "A 128 Gb/s PAM4 Silicon Microring Modulator With Integrated Thermo-Optic Resonance Tuning," *Journal of Lightwave Technology,* vol. 37, no. 1, pp. 110-115, 2019.

[7] D. Patel *et al.*, "Design, analysis, and transmission system performance of a 41 GHz silicon photonic modulator," *Opt. Express,* vol. 23, no. 11, pp. 14263-14287, 2015/06/01 2015.

[8] A. Samani *et al.*, "Highly Sensitive, 112 Gb/s O-band Waveguide Coupled Silicon-Germanium Avalanche Photodetectors," in *Optical Fiber Communication Conference (OFC) 2019*, San Diego, California, 2019: Optical Society of America, p. Th3B.1.

[9] X. Wang, Z. Cheng, K. Xu, H. K. Tsang, and J.-B. Xu, "High-responsivity graphene/silicon-heterostructure waveguide photodetectors," *Nature Photonics,* vol. 7, p. 888, 09/15/online 2013.

[10] A. Y. Liu, S. Srinivasan, J. Norman, A. C. Gossard, and J. E. Bowers, "Quantum dot lasers for silicon photonics [Invited]," *Photon. Res.,* vol. 3, no. 5, pp. B1-B9, 2015/10/01 2015.

[11] i.-e. SiPhotonics. *Passives technology* [Online]. Available: http://www.europractice-ic.com/SiPhotonics_technology_imec_passives.php.

[12] G. F. R. Chen, J. R. Ong, T. Y. L. Ang, S. T. Lim, C. E. Png, and D. T. H. Tan, "Broadband Silicon-On-Insulator directional couplers using a combination of straight and curved waveguide sections," *Scientific Reports,* vol. 7, no. 1, p. 7246, 2017/08/03 2017.

[13] H. Yun, W. Shi, Y. Wang, L. Chrostowski, and N. A. F. Jaeger, *2x2 Adiabatic 3-dB Coupler on Silicon-on-Insulator Rib Waveguides*. 2013.

[14] Z. Sheng *et al.*, "A Compact and Low-Loss MMI Coupler Fabricated With CMOS Technology," *IEEE Photonics Journal*, vol. 4, no. 6, pp. 2272-2277, 2012.

[15] A. S. Jugessur, J. Dou, J. S. Aitchison, R. M. De La Rue, and M. Gnan, "A photonic nano-Bragg grating device integrated with microfluidic channels for bio-sensing applications," *Microelectronic Engineering,* vol. 86, no. 4, pp. 1488-1490, 2009/04/01/ 2009.

[16] M. G. Saber *et al.*, "A CMOS Compatible Ultracompact Silicon Photonic Optical Add-Drop Multiplexer with Misaligned Sidewall Bragg Gratings," *IEEE Photonics Journal,* vol. 9, no. 3, pp. 1-10, 2017.

[17] D. Dai and H. Wu, "Realization of a compact polarization splitter-rotator on silicon," *Opt. Lett.,* vol. 41, no. 10, pp. 2346-2349, 2016/05/15 2016.

[18] Y. Wang *et al.*, "Compact single-etched sub-wavelength grating couplers for O-band application," *Opt. Express,* vol. 25, no. 24, pp. 30582-30590, 2017/11/27 2017.

[19] Y. Wang *et al.*, "Design of broadband subwavelength grating couplers with low back reflection," *Opt. Lett.,* vol. 40, no. 20, pp. 4647-4650, 2015/10/15 2015.

[20] C. Doerr *et al.*, "O, E, S, C, and L Band Silicon Photonics Coherent Modulator/Receiver," in *Optical Fiber Communication Conference Postdeadline Papers*, Anaheim, California, 2016: Optical Society of America, p. Th5C.4.

[21] H. Tamazin *et al.*, "Ultra-broadband Compact Adiabatic Coupler in Silicon-on-Insulator for Joint Operation in the C- and O-Bands," in *Conference on Lasers and Electro-Optics*, San Jose, California, 2018: Optical Society of America, p. STh4B.4.

[22] Y. Shani, C. H. Henry, R. C. Kistler, R. F. Kazarinov, and K. J. Orlowsky, "Integrated optic adiabatic devices on silicon," *IEEE Journal of Quantum Electronics,* vol. 27, no. 3, pp. 556-566, 1991.

[23] L. Xu *et al.*, "Polarization Independent Adiabatic 3-dB Coupler for Silicon-on-Insulator," in *Conference on Lasers and Electro-Optics*, San Jose, California, 2017: Optical Society of America, p. SF1I.5.

[24] H. Yun, Z. Lu, Y. Wang, W. Shi, L. Christowski, and N. A. F. Jaeger, "2×2 Broadband Adiabatic 3-dB Couplers on SOI Strip Waveguides for TE and TM modes," in *CLEO: 2015*, San Jose, California, 2015: Optical Society of America, p. STh1F.8.

[25] K. Solehmainen, M. Kapulainen, M. Harjanne, and T. Aalto, "Adiabatic and Multimode Interference Couplers on Silicon-on-Insulator," *IEEE Photonics Technology Letters,* vol. 18, no. 21, pp. 2287-2289, 2006.

[26] L. Cao, A. Elshaari, A. Aboketaf, and S. Preble, "Adiabatic couplers in SOI waveguides," in *CLEO/QELS: 2010 Laser Science to Photonic Applications*, 2010, pp. 1-2.

[27] H. Yun *et al.*, "Broadband 2 × 2 adiabatic 3 dB coupler using silicon-on-insulator sub-wavelength grating waveguides," *Opt. Lett.,* vol. 41, no. 13, pp. 3041-3044, 2016/07/01 2016.

[28] Y. Wang *et al.*, "Polarization-Independent Mode-Evolution-Based Coupler for the Silicon-on-Insulator Platform," *IEEE Photonics Journal,* vol. 10, no. 3, pp. 1-10, 2018.

[29] L. Xu *et al.*, "Compact high-performance adiabatic 3-dB coupler enabled by subwavelength grating slot in the silicon-on-insulator platform," *Opt. Express,* vol. 26, no. 23, pp. 29873-29885, 2018/11/12 2018.

[30] A. Y. a. P. Yeh, *Photonics: Optical Electronics in Modern Communications*, Sixth ed. (The Oxford series in Electrical and Computer Engineering). Oxford University Press, 2007.

[31] Y. Wang *et al.*, "Compact Broadband Directional Couplers Using Subwavelength Gratings," *IEEE Photonics Journal,* vol. 8, no. 3, pp. 1-8, 2016.

[32] K. Bergman, "Silicon Photonics For High Performance Interconnection Networks," in *Optical Fiber Communication Conference*, San Diego, California, 2018: Optical Society of America, p. Tu3F.1.

[33] S. Chen and D. Dai, "Ultra-broadband low-loss 2×2 MZI (Mach-Zehnder interferometer)-based thermo-optic switch with bent directional couplers on silicon," in *Optical Fiber Communication Conference*, Anaheim, California, 2016: Optical Society of America, p. M3I.4.

[34] J. V. Campenhout, W. M. J. Green, S. Assefa, and Y. A. Vlasov, "Low-power, 2×2 silicon electro-optic switch with 110-nm bandwidth for broadband reconfigurable optical networks," *Opt. Express,* vol. 17, no. 26, pp. 24020-24029, 2009/12/21 2009.

[35] M. R. Watts, J. Sun, C. DeRose, D. C. Trotter, R. W. Young, and G. N. Nielson, "Adiabatic thermo-optic Mach–Zehnder switch," *Opt. Lett.*, vol. 38, no. 5, pp. 733-735, 2013/03/01 2013.

[36] Á. Rosa, A. Gutiérrez, A. Brimont, A. Griol, and P. Sanchis, "High performace silicon 2x2 optical switch based on a thermo-optically tunable multimode interference coupler and efficient electrodes," *Opt. Express,* vol. 24, no. 1, pp. 191-198, 2016/01/11 2016.

[37] P. Dong *et al.*, "Submilliwatt, ultrafast and broadband electro-optic silicon switches," *Opt. Express,* vol. 18, no. 24, pp. 25225-25231, 2010/11/22 2010.

[38] Z. Lu, K. Murray, H. Jayatilleka, and L. Chrostowski, "Michelson Interferometer Thermo-Optic Switch on SOI With a 50-μW Power Consumption," *IEEE Photonics Technology Letters,* vol. 27, no. 22, pp. 2319-2322, 2015.

[39] M. Tran Anh, C. Zhang, and J. Bowers, *A broadband optical switch based on adiabatic couplers*. 2016, pp. 755-756.

[40] T. Kitoh, N. Takato, K. Jinguji, M. Yasu, and M. Kawachi, "Novel broad-band optical switch using silica-based planar lightwave circuit," *IEEE Photonics Technology Letters,* vol. 4, no. 7, pp. 735-737, 1992.

[41] M. A. Popović, E. P. Ippen, and F. X. Kärtner, "Universally balanced photonic interferometers," *Opt. Lett.*, vol. 31, no. 18, pp. 2713-2715, 2006/09/15 2006.

[42] T. E. Murphy, J. T. Hastings, and H. I. Smith, "Fabrication and characterization of narrow-band Bragg-reflection filters in silicon-on-insulator ridge waveguides," *Journal of Lightwave Technology,* vol. 19, no. 12, pp. 1938-1942, 2001.

[43] P. Y. Amnon Yariv, *Photonics: Optical electronics in Modern Communication*, Sixth Edition ed. Oxfor University Press, 2007.

[44] X. Wang, "Silicon Photonic Waveguide Bragg Gratings," Doctor of Philosophy, Electrical and Computer Engineering, University of British Columbia, 2013.

[45] X. Wang, W. Shi, H. Yun, S. Grist, N. A. F. Jaeger, and L. Chrostowski, "Narrow-band waveguide Bragg gratings on SOI wafers with CMOS-compatible fabrication process," *Opt. Express,* vol. 20, no. 14, pp. 15547-15558, 2012/07/02 2012.

[46] X. Wang *et al.*, "Precise control of the coupling coefficient through destructive interference in silicon waveguide Bragg gratings," *Opt. Lett.*, vol. 39, no. 19, pp. 5519-5522, 2014/10/01 2014.

[47] X. Wang *et al.*, "Lithography simulation for the fabrication of silicon photonic devices with deep-ultraviolet lithography," in *The 9th International Conference on Group IV Photonics (GFP)*, 2012, pp. 288-290.

[48] M. Burla *et al.*, "Terahertz-bandwidth photonic fractional Hilbert transformer based on a phase-shifted waveguide Bragg grating on silicon," *Opt. Lett.*, vol. 39, no. 21, pp. 6241-6244, 2014/11/01 2014.

[49] S. Srinivasan, A. W. Fang, D. Liang, J. Peters, B. Kaye, and J. E. Bowers, "Design of phase-shifted hybrid silicon distributed feedback lasers," *Opt. Express*, vol. 19, no. 10, pp. 9255-9261, 2011/05/09 2011.

[50] V. Jayaraman, Z. Chuang, and L. A. Coldren, "Theory, design, and performance of extended tuning range semiconductor lasers with sampled gratings," *IEEE Journal of Quantum Electronics*, vol. 29, no. 6, pp. 1824-1834, 1993.

[51] M. Morin, M. Poulin, A. Mailloux, F. Trepanier, and Y. Painchaud, "Full C-band slope-matched dispersion compensation based on a phase sampled Bragg grating," in *Optical Fiber Communication Conference, 2004. OFC 2004*, 2004, vol. 1, p. 740.

[52] X. Wang, W. Shi, R. Vafaei, N. A. F. Jaeger, and L. Chrostowski, "Uniform and Sampled Bragg Gratings in SOI Strip Waveguides With Sidewall Corrugations," *IEEE Photonics Technology Letters*, vol. 23, no. 5, pp. 290-292, 2011.

[53] I. Giuntoni, P. Balladares, R. Steingrüber, J. Bruns, and K. Petermann, "WDM Multi-Channel Filter Based On Sampled Gratings In Silicon-on-Insulator," in *Optical Fiber Communication Conference/National Fiber Optic Engineers Conference 2011*, Los Angeles, California, 2011: Optical Society of America, p. OThV3.

[54] N. N. Klimov, S. Mittal, M. Berger, and Z. Ahmed, "On-chip silicon waveguide Bragg grating photonic temperature sensor," *Opt. Lett.*, vol. 40, no. 17, pp. 3934-3936, 2015/09/01 2015.

[55] X. Wang *et al.*, "A silicon photonic biosensor using phase-shifted Bragg gratings in slot waveguide," *Journal of Biophotonics*, vol. 6, no. 10, pp. 821-828, 2013/10/01 2013.

[56] F. Ouellette, P. A. Krug, T. Stephens, G. Dhosi, and B. Eggleton, "Broadband and WDM dispersion compensation using chirped sampled fibre Bragg gratings," *Electronics Letters*, vol. 31, no. 11, pp. 899-901, 1995.

[57] I. Giuntoni *et al.*, "Integrated drop-filter for dispersion compensation based on SOI rib waveguides," in *2010 Conference on Optical Fiber Communication (OFC/NFOEC), collocated National Fiber Optic Engineers Conference*, 2010, pp. 1-3.

[58] D. T. H. Tan, K. Ikeda, and Y. Fainman, *Coupled chirped vertical gratings for on-chip group velocity dispersion engineering*. 2009, pp. 141109-141109.